Dynamic full-field imaging of rupture radiation: Material contrast governs source mechanism

Aichele Johannes[1], latour soumaya[2], Catheline Stefan[3], and Roux Philippe[4]

[1]Swiss Federal Institute of Technology in Zurich
[2]Université Toulouse 3 - Paul Sabatier
[3]Lyon 1 University - INSERM
[4]Université Grenoble Alpes & CNRS

November 16, 2022

Abstract

In seismology, the rupture mechanism of an earthquake, a glacier stick-slip and a landslide is not directly observed, but inferred from surface measurements. In contrast, laboratory experiments can illuminate near field effects, which reflect the rupture mechanism but are highly attenuated in the case of real-world surface data. We directly image the elastic wave-field of a nucleating rupture non-invasively in its near-field with ultrasound speckle correlation. Our imaging yields the particle velocity of the full shear wave field at the source location and inside the 3D frictional body. We experimentally show that a strong bimaterial contrast, as encountered in environmental seismology, yields a unidirectional or linear force mechanism for pre-rupture microslips and decelerating supershear ruptures. A weak contrast, characteristic for earthquakes, generates a double-couple source mechanism for sub-Rayleigh ruptures, sometimes preceded by slow deformation at the interface. This deformation is reproduced by the near field of a unidirectional force.

Dynamic full-field imaging of rupture radiation: Material contrast governs source mechanism

Aichele J.[1,2*], Latour S.[3], Catheline S.[1], and Roux P.[2]

[1]Laboratory of Therapeutic Applications of Ultrasound, INSERM & University of Lyon, Lyon, France
[2]ISTerre, Univ. Grenoble Alpes, Univ. Savoie Mont Blanc, CNRS, IRD, Univ. Gustave Eiffel, Grenoble, France
[3]Institute of Astrophysics and Planetology, IRAP & University of Toulouse III, Toulouse, France

*currently at Department of Earth Sciences, Institute of Geophysics, Swiss Federal Institute of Technology, Zürich, Switzerland

Corresponding author: Aichele J., `johannes.aichele@rwth-aachen.de`

Abstract

In seismology, the rupture mechanism of an earthquake, a glacier stick-slip and a landslide is not directly observed, but inferred from surface measurements. In contrast, laboratory experiments can illuminate near field effects, which reflect the rupture mechanism but are highly attenuated in the case of real-world surface data. We directly image the elastic wave-field of a nucleating rupture non-invasively in its near-field with ultrasound speckle correlation. Our imaging yields the particle velocity of the full shear wave field at the source location and inside the 3D frictional body. We experimentally show that a strong bimaterial contrast, as encountered in environmental seismology, yields a unidirectional or linear force mechanism for pre-rupture microslips and decelerating supershear ruptures. A weak contrast, characteristic for earthquakes, generates a double-couple source mechanism for sub-Rayleigh ruptures, sometimes preceded by slow deformation at the interface. This deformation is reproduced by the near field of a unidirectional force.

Key Points:

- Noninvasive elastic near-field laboratory observations reveal source mechanisms of micro-slips, supershear and sub-Rayleigh ruptures.
- Strong material contrasts as encountered in glacier stick-slip and landslides cause single force micro-slips and supershear ruptures.
- Weak material contrasts lead to a double-couple mechanism, sometimes preceded by the near field radiation of a slowly rising single force.

Plain Language Summary

Earthquakes, avalanches, icequakes and landslides originate from a common process: rupture at a material interface. During a rupture, for example when a landslide slips, a characteristic pattern of seismic waves is created. This pattern differs at the earth's surface and the rupture interface, which is the source of the seismic waves inside the earth. Usually scientists only measure the waves arriving at the surface and need to deduce the wave pattern inside the earth from the surface measurement. We build a laboratory experiment which enables us to film wave propagation around the rupture surface, as if we had a camera inside the material. We film waves emitted during and prior to a rupture. For a soft material on a hard surface, such as encountered in icequakes or landslides, a single force model better explains the observed wave pattern than the commonly used model of four distributed forces. The rupture moves faster than shear waves propagate which results in a supershear cone, the elastic equivalent to the acoustic Mach cone created by supersonic aircrafts. For two materials of similar hardness, such as encountered in earthquakes, the classic model of four forces better explains the ruptures, which travel at sub-shear speed.

1 Introduction

For most earthquakes, the longstanding discussion on the appropriate force representation of the earthquake source has been decided in favor of the double-couple (DC) source. It is the body force equivalent to slip on a fault and consists of two force couples acting at the earthquake source point (Pujol, 2003; Aki & Richards, 2009). However, other rupture observations such as icequakes, landslides, induced seismicity and deep earthquakes are not always well reproduced by a standard double-couple model. For example, Ben-Zion and Ampuero (2009) theoretically show that brittle rupture is associated with a non-double-couple damage related source term. Kwiatek et al. (2011); Kwiatek and Ben-Zion (2013) discuss the presence of tensile opening during induced seismicity and aftershocks of a Mw

1.9 earthquake. In the case of glacial sliding, Ekström et al. (2003) report that a single force centroïd inversion shows a better match than standard moment tensor inversion (Harvard-CMT). In the laboratory, Lykotrafitis and Rosakis (2006) found indications for wrinkle-like rupture and tensile opening in a Homalite-on-steel friction experiment.

Inversion for earthquake sources is mostly done in the far-field and suffers from ambiguity. With the exception of volcanic seismicity, where hypocenters are shallow (Lokmer & Bean, 2010), the seismic near field suffers strong attenuation and is often concealed by ambient noise. In contrast to real-world seismic data, laboratory rupture experiments allow for dense instrumentation and direct imaging of rupture propagation. For example, the first unambiguous proof of supershear rupture was provided by strain imaging through photo-elastic experiments of sliding Homalite plates by Rosakis and Coker (1999). Recently, the group retrieved wave motion displacements of supershear ruptures through digital image correlation (Rubino et al., 2020, 2022). Latour et al. (2011, 2013) introduced a new direct rupture imaging method using ultrafast ultrasound imaging that allows for observation of shear wave radiation during rupture propagation in soft materials: the particle velocity of a propagating shear wave is retrieved through speckle tracking of subsequent ultrasound (US) backscatter images. In contrast to photo-elasticity, this method is not restricted to 2D setups. Their results show that during hydrogel-on-sandpaper friction the depinning of the gel from the sandpaper is well matched by a singular bell shaped (Gaussian) shear point force. They also directly observed the effects of barriers on rupture propagation on a hydrogel-glass interface with a granular inter-layer. At first glance hydrogels might seem counterintuitive as a material choice in rupture experiments. However, they have been extensively used as geological analogues (van Otterloo & Cruden, 2016). An historic example is the jelly experiment of Reid (1910) that led to the elastic rebound theory. More recent examples include a subduction-analogue gelatin setup (Corbi et al., 2011),(Corbi et al., 2017) and volcanic modeling (Kavanagh et al., 2018).

Here we investigate the source mechanism of the failure of a granular asperity in a laboratory friction experiment using a new setup based on the methodology introduced by Latour et al. (2011, 2013). Direct imaging of the near field of a propagating rupture allows us to compare the laboratory rupture to a kinematic rupture simulation using elastodynamic Green's functions. We compare the case of weak and strong bimaterial contrast and test single-force and double-couple source models to find the source mechanism depending on the elastic contrast and type of slip event.

Experimental setup

All results are derived from the dynamic wave field imaging of two experimental scenarios: sliding of an asperity along an interface with a strong or a weak bimaterial contrast (Fig. 1). The strong bimaterial contrast is constituted of a glass - hydrogel (Polyvinyl-alcohol - PVA) interface (Fig. 1(a)-(b)) and the weak bimaterial contrast by a hydrogel-hydrogel interface (Fig. 1(d)). Since the hydrogels are homemade and non-standardized, an elasticity contrast has to be assumed between them. The frictional behaviour is ensured by a sand patch mimicking an asperity on a smooth surface. The glass plate is moved by a Kollmorgen stepper motor, which induces the deformation then subsequent sliding of the partly blocked gel via the frictional contact of the sand asperity. Seismic radiation is emitted upon failure of frictional contacts due to stick-slip ruptures, and is observed by ultrasonic speckle correlation imaging. The observation plane is centered in the gel, perpendicular to the interface and reaches from the asperity to the gel surface.

The imaging methodology is exemplary shown in Fig. 1(c) with data from the weak interface experiment. Ultrasound backscatter images show a zone of high reflectivity at the gel-gel interface at 4 cm depth. It is caused by the sand layer and the presence of air in between the two hydrogels. Imaging below the interface is feasible, but the speckle quality is deteriorated due to strong ultrasound backscattering. In both gels, a 1 cm thick layer of intermediate reflectivity is observed next to the sand. It is likely caused by increased deposition of the backscatter agent (graphite). While graphite changes the ultrasonic impedance, shear wave propagation at the frequencies of interest remains unaffected. The phase correlation of successive ultrasound speckle images allows to resolve the shear wave induced vertical particle displacement between two snapshots, which is the apparent particle velocity $\frac{\partial u_z}{\partial t}$ (Pinton et al., 2005).

The dynamic observation is made possible by the high velocity contrast of the shear and compression waves in the hydrogel: while the compressional ultrasound travels at approximately $1500\,\mathrm{m\,s^{-1}}$, the rupture induced shear waves propagate at speeds below $10\,\mathrm{m\,s^{-1}}$. Plane ultrasound pulses at high frame rate allow for the shear wave particle velocity to be temporally well resolved ($\Delta_t = 0.33\,\mathrm{ms}$). The ultrasound frequency ($5\,\mathrm{MHz}$) ensures the spatial resolution ($\lambda_{US} = 0.3$ mm). Hence, a shear wave propagating at $7\,\mathrm{m\,s^{-1}}$ and $250\,\mathrm{Hz}$ is sampled at 25 US-wavelengths per shear wavelength ($\lambda_{shear} = 7$ mm). Consequently, the z-component of the entire transverse displacement field, including near-field terms, is observed.

Kinematic modeling of the radiated wavefield

The observed wavefields radiated by the slip events are compared to direct kinematic wavefield modeling of equivalent body-force models (see section S2.6-S2.8) In each case, we compare the single-force and the douple-couple solutions. The source moves to simulate propagation of rupture fronts, and its velocity as well as the local source time functions are manually adjusted to obtain a good match to the data.

The displacement $u_{ij}(x,t)$ due to a unidirectional force (UF) in the x_j-direction with a source time function $X_0(t)$ at the source position is the convolution of X_0 with the elastodynamic impulse response (Green's function G_{ij}). It is the superposition of the compression and shear wave far-fields and the elastic near-field:

$$\begin{aligned} u_i(\vec{x},t) =& X_0 * G_{ij} \\ =& X_0 * {G_{ij}}^{Near} + X_0 * {G_{ij}}^{Far-P} + X_0 * {G_{ij}}^{Far-S} \end{aligned} \tag{1}$$

The full expression is given in Section S2.6 and a thorough derivation can be found in Aki and Richards (2009) Chapter 3-4.

In contrast to the UF-solution in Eq. (1), the Green's function for a double-couple (DC) model can be separated into five physically meaningful terms: Near-field, intermediate S-field and P-field, and far S-field and P-field.

$$G_{DC} = G^{Near} + G^{IP} + G^{IS} + \quad G^{FP} + G^{FS} \tag{2}$$

The full analytical solution for the displacement field of a DC source can be found in Section S2.7.

In the following, we first present the results on the strong and weak contrast bimaterial interface and then discuss their relevance for natural rupture processes.

Strong bimaterial contrast

The wavefield observations for the strong bimaterial contrast (movie S1) reveals two types of slip events at the asperity: strongly localized micro-slips, and moving rupture fronts that propagate along the asperity and cause a global stick-slip behaviour (see fig S6). We analyze one event of each type, representative of the overall observations.

For the microslip event, depicted in Fig. 2(a), a spherical wavefront is radiated from one location on the asperity. No rupture propagation is observed and consequently we model the

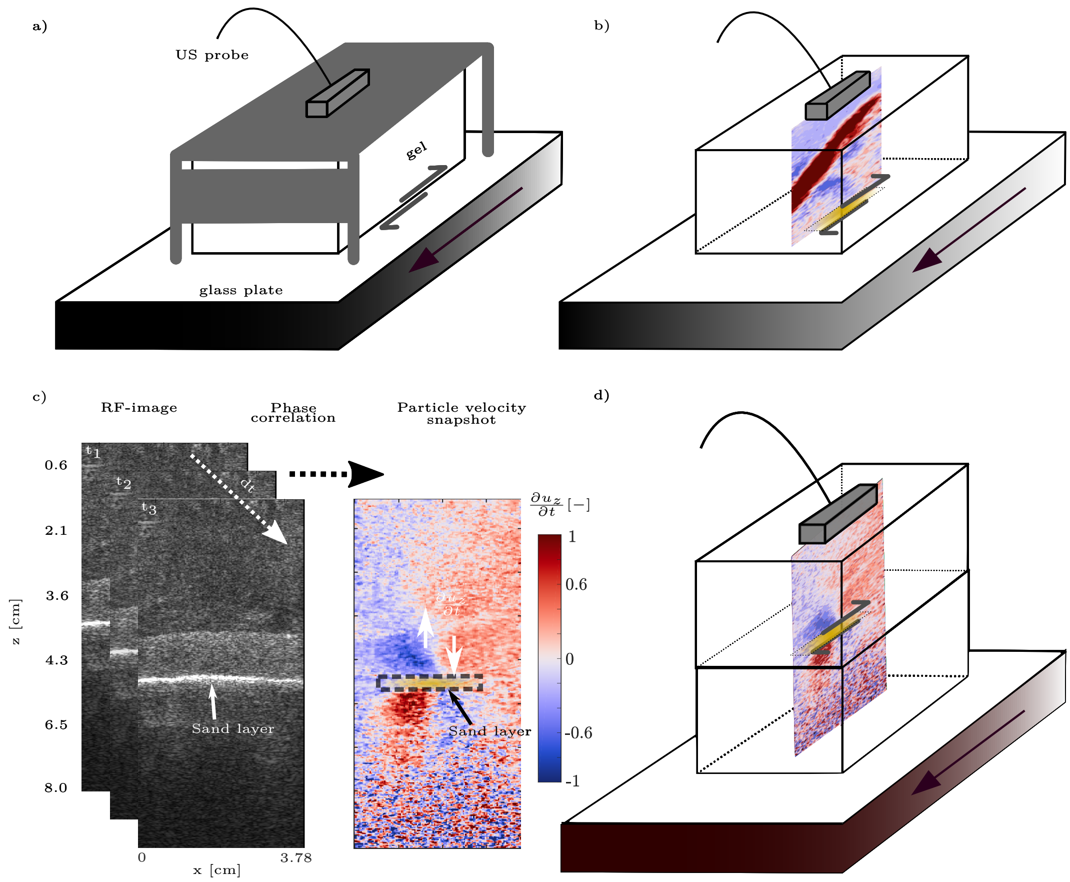

Figure 1. Experimental setup and imaging methodology. (a) Schematic view of the montage. The gel is free at the interface and blocked above. (b) Imaging methodology: Correlation of successive US reflection images results in retrieval of the vertical component of the shear wave's particle velocity. Blue denotes upwards polarization (negative z) and red denotes downwards polarization (positive z). (b) and (d) Schematic illustration of the imaging plane in the bimaterial setups: (b) A hydrogel - sand asperity - glass interface constitutes the strong bimaterial contrast. (d) A hydrogel - sand asperity - hydrogel constitutes the weak bimaterial contrast. A detailed acquisition and processing workflow is given in Fig. S1.

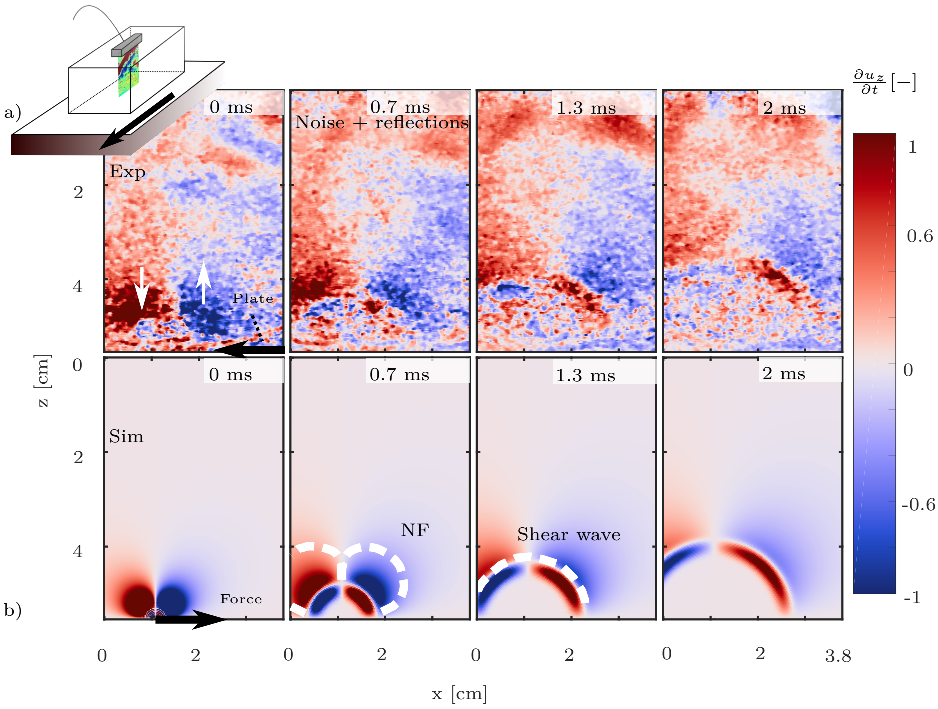

Figure 2. Strong material contrast: Comparison of an experimental micro-slip and simulation. Particle velocity direction is indicated by the white arrows. (a) Particle velocities $\frac{\delta u_z}{\delta t}$ observed by shear wave imaging. The stepper motor drives the plate in negative x-direction. (b) Complete Green's function for displacement u_z of a singular unidirectional shear force in positive x-direction. A median filter was applied to visually highlight the coherent wavefronts. All images are scaled by their extreme values. The near field lobe (NF) and shear wave front are indicated in panels (b).

event with a local point source. The experimental radiation pattern is well reproduced by a unidirectional single force model, as shown in Fig. 2(b) using a ramp shaped source time function $X_0(t)$. The first lobe represents the near field (NF) lobe of the Green's function and is quickly attenuated. The second lobe is of opposite polarity and represents the far-field shear wave. The top 2 cm are artifacts of a previous event (see Fig. S2 event 2-3). In contrast to the simulation, the experiment undergoes constant charging from the motor. Thus, noise as well as aseismic displacement due to deformation are present in the snapshots.

The gaussian source time function of the force employed by Latour et al. (2011) to model depinning events of hydrogel on sand paper fails to reproduce the here observed wavefield. Our ramp shaped source time function with rise time of 0.1ms (see Fig. S10) results in a better match. The plate displacement deforms the gel and a likely physical explanation is a localized change from a high- to low-stress state, which we model by a ramp function in time of a rightward point force (see Fig. S10). Dynamically, this is equivalent a left-pointing loading force applied to the gel, which drops to zero value, corresponding to a shear friction drop localized on a micro-asperity. In the granular layer it might correspond to a highly localized inelastic dislocation or grain micro-slip.

The localized event of Fig. 2 precedes a larger event, in which a rupture front traverses the entire visible interface (see Fig. 3 (a) and Figs. S3-S4 for details). The rupture propagation direction equals the sliding direction of the gel, *i.e.* opposite to the plate movement. This observation agrees with Dedontney et al. (2011), who found that for bimaterial interfaces, ruptures will preferentially propagate in slip direction of the compliant side. The particle velocity ($\frac{\delta u_z}{\delta t}$) measurements in Fig. 3 (a) are compared to two analytic, kinematic simulations: a moving unidirectional force (UF) Fig. 3(b), and a moving double-couple (DC) Fig. 3(c). The simulations result from superposition of point sources along a decelerating speed profile, which is estimated roughly from the experimental data. Through trial and error we qualitatively match the near field lobe, supershear- and rupture arrest front. The source parameters are given in Figs. S10-S14.

Key properties of the unidirectional force model, which are also present in the experimental observation, are indicated in Fig. 3 (b). The first phase is an upwards polarized non-planar lobe with a diffuse front. It corresponds to the near-field (NF) of the right-traveling and rightwards pointing shear force. A sharp, downwards polarized large amplitude wave front follows, which is identified as a supershear front in the simulation. It is the result of a rupture that breaks the asperity faster than the medium's shear wave speed. The front angle with the x-axis (β=21.8°) at late observation times in Fig. 3 (a) and the measured shear wave speed (c_s) of $6.9\,\mathrm{m\,s^{-1}} \pm 1\,\mathrm{m\,s^{-1}}$ (see Fig. S15) are used to calculate an average rupture propagation speed (c_r) of $\approx 18\,\mathrm{m\,s^{-1}}$: $c_r = \frac{c_s}{sin(\beta)}$. However, two front angles can be identified throughout the rupture (see Fig. S17). Furthermore, a time of flight measurement of the supershear front along the rupture surface (see Fig. S16) suggests a rupture speed above time resolution on 1 cm and below $12\,\mathrm{m\,s^{-1}}$ afterwards, indicating that the rupture is decelerating. This justifies the use of a decreasing rupture velocity in the kinematic model. A low amplitude, downwards polarized wedge is present above the supershear front. It corresponds to the imprint of the compressional (P) wave, which propagates at $\approx 1500\,\mathrm{m\,s^{-1}}$. Finally, a leftwards propagating and upwards polarized wavefront can be observed in the last snapshots of Fig. 3 (a). In the simulations it is identified as the rupture arrest front (RAF), emitted at the asperity border.

In comparison, the best moving DC solution(Fig. 3 (c)) exhibits a high wavefield complexity which is absent in the experiment and in the UF force simulation. Furthermore, the experimental data lack the leading, downwards polarized polarity of the DC simulation. However, at late times (7 ms), we can observe an upwards polarized front following the supershear front, which has a counterpart in the DC solution (Fig. 3 (c)), but is absent in the UF simulation Fig. 3 (b). To conclude, we find that the moving unidirectional force better matches the near field,the supershear front and the rupture arrest front of the experimental data than the double couple model, but does not capture every detail of the wavefield.

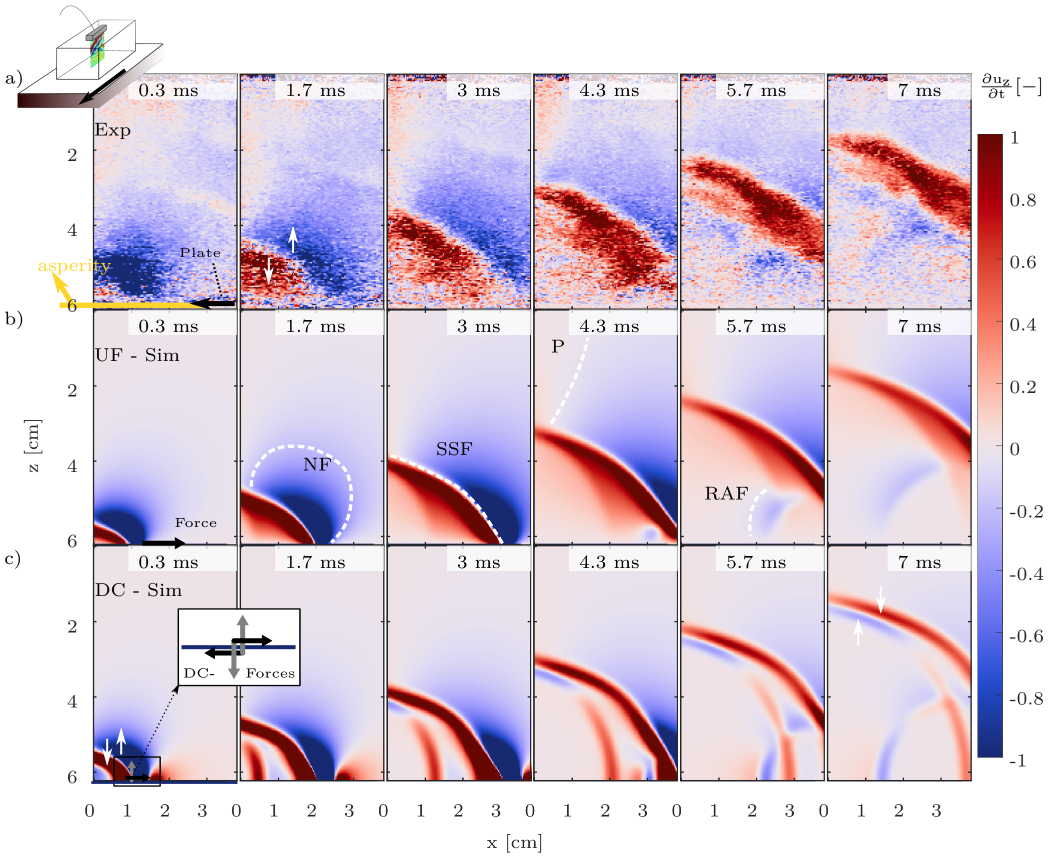

Figure 3. Strong material contrast: Comparison of an experimental supershear rupture and simulation. a) $\frac{\delta u_z}{\delta t}$ as observed by shear wave imaging. The rupture follows the event of Fig. 2. The first snapshot is located 6 ms after the first snapshot of Fig. 2. The motor drives the plate in negative x-direction. b) $\frac{\delta u_z}{\delta t}$ resulting from the superposition of unidirectional shear forces in x-direction. Near field (NF), supershear front (SSF), P-wave imprint (P) and rupture arrest front (RAF) are indicated. c) $\frac{\delta u_z}{\delta t}$ resulting from the superposition of double-couple point sources. The point sources in b) and c) are shifted in time and space, in order to simulate the horizontal advancement of a rupture front (see Supplementary material Section 2.8). All snapshots are normalized with respect to their time-series. The sources are directed in positive x-direction. A higher time-resolution is given in Figs. S4-S5. The source functions and rupture speed profiles can be found in Figs. S11-S12.

Weak bimaterial contrast

We observe again two types of slip events on the weak bimaterial contrast interface: propagating ruptures and localized wave radiations (see movie S2).

A rupture that appears to propagate below shear and Rayleigh wave speed is shown in Fig. 4 (a). Rupture propagation at sub-Rayleigh speed is expected for homogeneous systems (Shlomai & Fineberg, 2016), but has not been observed by shear wave imaging prior to this observation, which is the first dynamic US observation of a gel-gel rupture (Latour et al., 2011). Fig. 4 (c)-(d) show the corresponding 1D waveforms at specified depth- and time-steps in the upper halfspace. In both displays, the right-traveling front exhibits higher amplitudes than the left-traveling one. This front also exposes a smaller angle to the vertical (inclination difference), indicating a speed difference between the fronts. A straightforward explanation is a right-travelling sub-Rayleigh rupture. A wavefront of continuous polarity throughout both half-spaces exists in the rupture propagation direction.

We model the radiation with a double-couple moving to the right at constant sub-Rayleigh velocity (Fig. S13). The simulated wavefield (Fig. 4 (b)-(e)-(f)) reproduces the continuous polarity across the interface. In contrast, the radiation pattern of a unidirectional force exhibits alternating polarities in the two halfspaces (Fig. S9). However, similar to the case of a strong bimaterial contrast, the leading near-field lobe predicted by the double-couple solution is not identified in the experimental data. Fig. 4 a) reveals that a weak upwards polarized zone is present at interface depth, but quickly disappears with depth. This could be an imprint of the near field which gets masked by the continuous deformation of the gel (see movie S2, (Figs. 4 and 5 start at approximately 2396 ms)). Note that the amplitude increase in the rupture direction is reproduced but more pronounced in the simulation than in the experiment. The experiment suffers from shear wave attenuation which is neglected in the kinematic simulation and might mask the amplitude difference between the front in rupture direction and the radiation front in opposite direction. Furthermore, the laboratory rupture might be shorter than the qualitatively simulated rupture of Fig. 4 (b).

Situated three milliseconds after Fig. 4, Fig. 5 (a) shows a localized event with a quadripolar radiation pattern (see Fig. S8 for a comprehensive time-series). The radiation is qualitatively reproduced as the near-field lobe of a unidirectional point force model, which is shown in Fig. 5(b). The source rise time is several ms long (see Fig. S13). Contrary to the localized event on the strong bimaterial contrast interface, the far-field part of the theoretical force radiation is not observed. Instead, the event is followed by a left-going rupture, shown in Fig. 5 (c) (event 3 in Fig. S8). A similar sequence can be observed at 2350 ms in movie S2. One hypothesis is that the long rise-time localized event corresponds to the nucleation process of the subsequent rupture. There appears to be an aseismic lateral displacement of the radiation pattern in the lower half space for the experimental data of unclear origin.

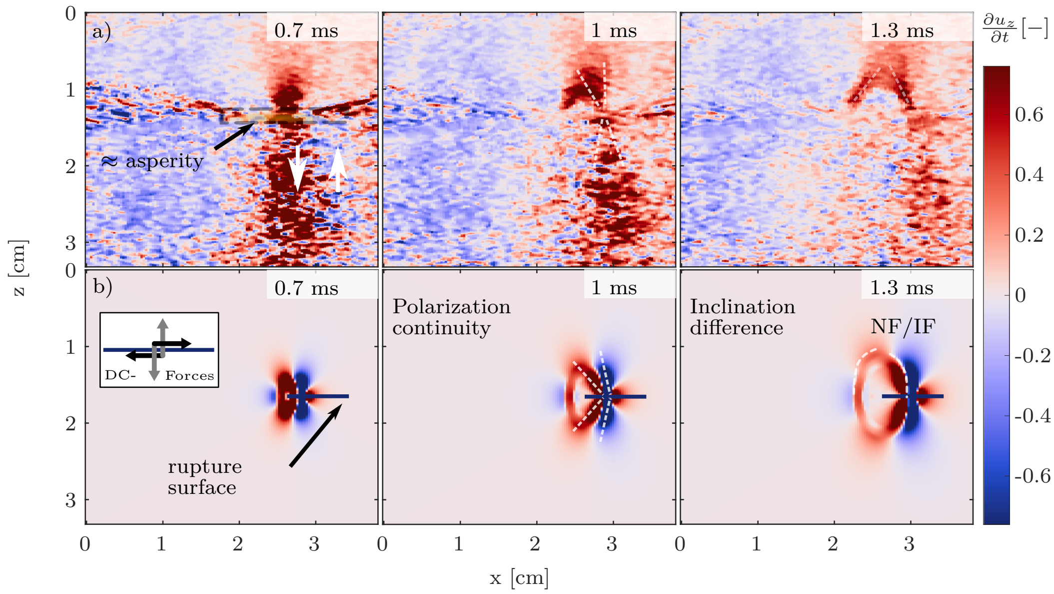

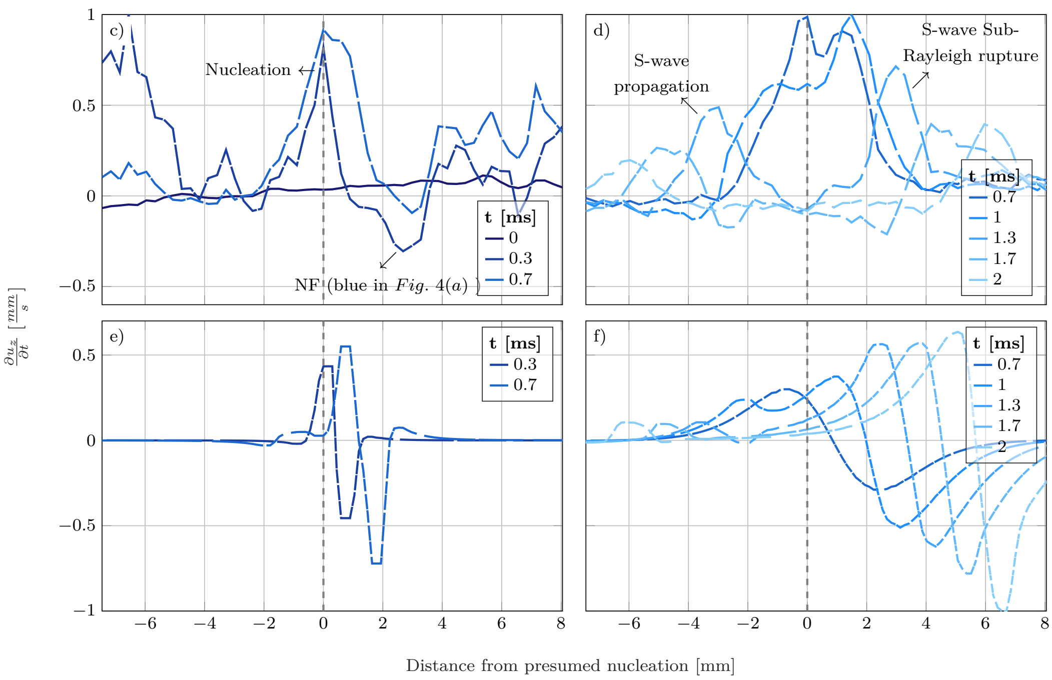

Figure 4. Weak material contrast: Comparison of an experimental sub-Rayleigh rupture and simulation. (a) Experimental particle velocities for a gel-gel rupture. (b) Right-traveling superposition of DC point sources at sub-Rayleigh speed with a ramp source function. The DC-force directions are indicated. The leading near and intermediate fields are indicated as NF/IF. (c)-(f) Spatial Waveforms (x-direction) at fixed depth and time plotted against the distance to the presumed rupture nucleation point. (c) Experimental waveforms during rupture initiation (0 ms - 0.7 ms) at the gel-gel interface. The waveforms are a mean of 27 depthpoints (≈1 mm), just above the sand layer, which was identified from the US reflection images. The relative position of the sand layer to the probe varies about 1.5 mm due to gel deformation and sand thickness. (d) Experimental waveforms of 0.7 to 2 ms ≈ 2 mm above the waveforms in (c). (e) - (f) Simulated waveforms corresponding to (c) and (d). (e) is taken 0.2 mm and (f) 3.8 mm above the simulated interface.

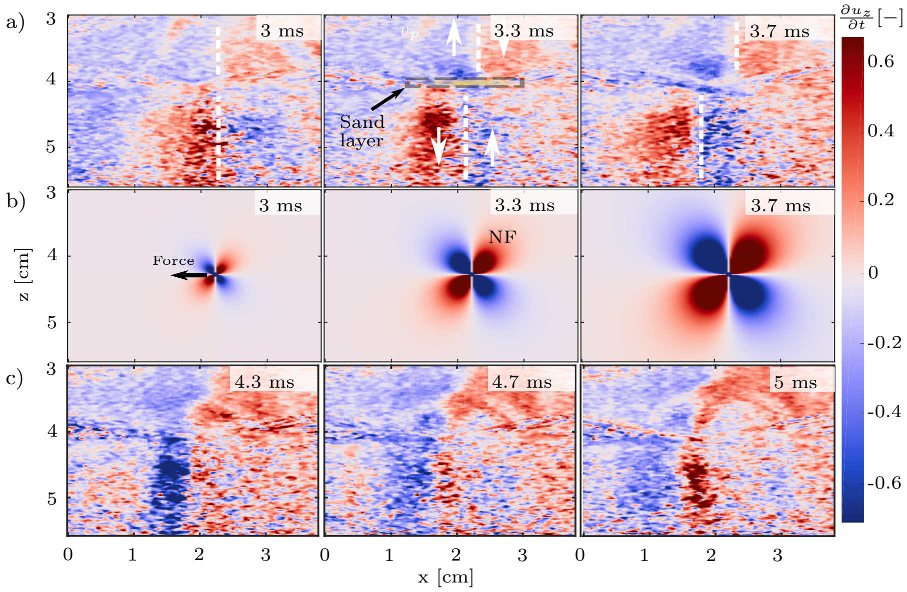

Figure 5. Weak bimaterial contrast: Comparison of an a local event and a UF-simulation. a) The interface is identified by the separation of the upper and lower lobes. Note that imaging quality is deteriorated by US diffraction at the sand, visible in the diagonal artifact in $t = 3$ms and the coarse appearance of the displacement field below the frictional interface. The event happens 3 ms after the rupture shown in Fig. 4. b) Green's function simulation of a localized unidirectional shear force in negative x-direction using a 2.16 ms long rise time for the Gaussian. The near field lobe is indicated as NF. c) Consequent time evolution of (a). The local event is followed or transforms into a rupture (see movie S2 $\approx$ 2400 ms).

Relevance for natural rupture processes

For the strong bimaterial contrast, we find that microslip events as well as propagating ruptures radiations are better described by a unique force model than by a double couple model. This is intuitively understood as due to the strong elastic contrast at the interface: the unidirectional force corresponds to the relaxation of the gel's loading force when friction drops at the interface.

In nature, strong material contrasts are encountered in environmental seismology, i.e. for landslides and glacier stick-slip. Both processes exhibit a wet granular layer and a compliant mass sliding on a hard bedrock. Our granular asperity is conceptually comparable to the "sticky spot" encountered in alpine glacial stick-slip (Umlauft et al., 2021). Unidirectional force source models have been proposed for the 1980 Mt. St. Helens eruption (Kanamori & Given, 1982) and the 1975 Kalapana, Hawaii, earthquake, where a large landslide occurred on Kilauea volcano(Eissler & Kanamori, 1987). In a theoretical analysis Dahlen (1993) showed that a lower shear wave velocity in the brecciated sliding block of shallow landslides results in mechanical decoupling of the two fault sides. The decoupling leads to a single-force rupture source, with the force pointing in the direction of the mass movement for decelerating sliding (Julian et al., 1998). Ekström et al. (2003) found that for glacier stick-slip in Greenland, single force inversions perform better than standard moment tensor inversions. Again, this could be explained by the lower shear wave speed in ice. Lastly, Trottet et al. (2022) very recently showed rupture propagation at supershear speed for snow avalanches, another case exposing low shear wave speeds of the sliding mass ($< 120\,\mathrm{m\,s^{-1}}$). We confirm through direct experimental observation of the wavefield generation that unique force mechanisms are relevant for describing slip events between two materials with strong wave velocity contrasts.

In global seismology, the earthquake source corresponds to slip on a planar fault and is widely modeled by a double couple equivalent body source. Our closest analogue experiment is the case of the propagating rupture on the asperity at the gel-gel interface. We observe radiations best described by a moving double couple , which indicates a symmetry in the strain relaxation process and a coupling between both sides of the fault. However, some ruptures are preceded by localized events which can be described by the near-field radiation of a slowly rising unidirectional force, even though the materials are almost symmetric. We hypothesize that one gel is more deformed than the other during loading. It then begins to relax slowly as a preparatory process before rupture propagation initiation and both gels relax the remaining deformation. This non-symmetric process may be possible thanks to the presence of the sand layer than can locally decouple both sides of the fault through grain rearrangements. The single force source mechanism may be relevant for slow processes on natural faults. Shallow thrust faults for example expose an asymmetry in the fault loading, and fault gouge, damaged layers and fluids can constitute a decoupling mechanism.

Acknowledgements

We are grateful to Christophe Voisin for discussions on rupture nucleation and Max Solazzo for finishing the friction bench. The project has received funding from the European Union's Horizon 2020 research and innovation programme under the Marie Sklodowska-Curie grant agreement No 641943 (ITN WAVES) and resulted in the PHD thesis Aichele (2019). ISterre is part of Labex OSUG@2020.

Open Research section

Data archiving is currently underway and will be archived at: `https://zenodo.org`. Temporary access has been granted via ETH polybox:
`https://polybox.ethz.ch/index.php/s/0r8J638Hs8vlDa0`

References

Aichele, J. (2019). *Elastic waves in complex conditions : From the onset of rupture to viscous dispersion in foams* (Doctoral dissertation, Université de Lyon). Retrieved 2022-01-05, from https://tel.archives-ouvertes.fr/tel-02481746

Aki, K., & Richards, P. G. (2009). Quantitative seismology. In *Book* (Second ed., p. 700). University Science Books. Retrieved from http://books.google.com/books?id=sRhawFG5_EcC&printsec=frontcover%5Cnpapers2://publication/uuid/A2074D09-FE3A-4600-9E91-CA393C8AF127

Ben-Zion, Y., & Ampuero, J.-P. (2009, September). Seismic radiation from regions sustaining material damage. *Geophysical Journal International*, *178*(3), 1351–1356. Retrieved 2022-01-05, from 10/d92gs8 doi: 10/d92gs8

Corbi, F., Funiciello, F., Brizzi, S., Lallemand, S., & Rosenau, M. (2017). Control of asperities size and spacing on seismic behavior of subduction megathrusts. *Geophysical Research Letters*, *44*(16), 8227–8235. doi: 10.1002/2017GL074182

Corbi, F., Funiciello, F., Faccenna, C., Ranalli, G., & Heuret, A. (2011, June). Seismic variability of subduction thrust faults: Insights from laboratory models. *Journal of Geophysical Research*, *116*(B6), B06304. Retrieved from http://doi.wiley.com/10.1029/2010JB007993 doi: 10.1029/2010JB007993

Dahlen, F. A. (1993, February). Single-force representation of shallow landslide sources. *Bulletin of the Seismological Society of America*, *83*(1), 130–143. Retrieved 2022-01-17, from https://doi.org/10.1785/BSSA0830010130 doi: 10/gn47cq

Dedontney, N., Templeton-Barrett, E. L., Rice, J. R., & Dmowska, R. (2011). Influence of plastic deformation on bimaterial fault rupture directivity. *Journal of Geophysical Research: Solid Earth*, *116*(10). doi: 10.1029/2011JB008417

Eissler, H. K., & Kanamori, H. (1987). A single-force model for the 1975 Kalapana, Hawaii, Earthquake. *Journal of Geophysical Research: Solid Earth*, *92*(B6), 4827–4836. Retrieved 2022-07-08, from https://onlinelibrary.wiley.com/doi/abs/10.1029/JB092iB06p04827 doi: 10.1029/JB092iB06p04827

Ekström, G., Nettles, M., & Abers, G. A. (2003, October). Glacial Earthquakes. *Science*. Retrieved 2022-01-05, from 10.1126/science.1088057 doi: 10/cxjwhc

Julian, B. R., Miller, A. D., & Foulger, G. R. (1998). Non-double-couple earthquakes 1. Theory. *Reviews of Geophysics*, *36*(4), 525–549. Retrieved 2022-01-05, from 10/dwdfzv doi: 10/dwdfzv

Kanamori, H., & Given, J. W. (1982). Analysis of long-period seismic waves excited by the May 18, 1980, eruption of Mount St. Helens—A terrestrial monopole? *Journal of Geophysical Research: Solid Earth*, *87*(B7), 5422–5432. Retrieved 2022-07-08, from https://onlinelibrary.wiley.com/doi/abs/10.1029/JB087iB07p05422 doi: 10.1029/JB087iB07p05422

Kavanagh, J. L., Engwell, S. L., & Martin, S. A. (2018, April). A review of laboratory and numerical modelling in volcanology. *Solid Earth*, *9*(2), 531–571. Retrieved 2022-06-15, from https://se.copernicus.org/articles/9/531/2018/ doi: 10.5194/se-9-531-2018

Kwiatek, G., & Ben-Zion, Y. (2013, July). Assessment of P and S wave energy radiated from very small shear-tensile seismic events in a deep South African mine. *Journal of Geophysical Research: Solid Earth*, *118*(7), 3630–3641. Retrieved from http://doi.wiley.com/10.1002/jgrb.50274 doi: 10.1002/jgrb.50274

Kwiatek, G., Plenkers, K., & Dresen, G. (2011). Source parameters of picoseismicity recorded at Mponeng deep gold mine, South Africa: Implications for scaling relations. *Bulletin of the Seismological Society of America*, *101*(6), 2592–2608. doi: 10.1785/0120110094

Latour, S., Gallot, T., Catheline, S., Voisin, C., Renard, F., Larose, E., & Campillo, M. (2011). Ultrafast ultrasonic imaging of dynamic sliding friction in soft solids: The slow slip and the super-shear regimes. *EPL (Europhysics Letters)*, *96*(January 2016), 59003. doi: 10.1209/0295-5075/96/59003

Latour, S., Voisin, C., Renard, F., Larose, E., Catheline, S., & Campillo, M. (2013). Effect of fault heterogeneity on rupture dynamics : An experimental approach using ultrafast ultrasonic imaging. *Journal of Geophysical Research: Solid Earth*, *118*(11), 5888–5902. Retrieved from http://scitation.aip.org/content/asa/journal/jasa/130/4/10.1121/1.3655012 doi: 10.1002/2013JB010231

Lokmer, I., & Bean, C. J. (2010, April). Properties of the near-field term and its effect on polarisation analysis and source locations of long-period (LP) and very-long-period (VLP) seismic events at volcanoes. *Journal of Volcanology and Geothermal Research*, *192*(1-2), 35–47. Retrieved 2022-05-09, from https://linkinghub.elsevier.com/retrieve/pii/S0377027310000521 doi: 10.1016/j.jvolgeores.2010.02.008

Lykotrafitis, G., & Rosakis, A. J. (2006). Dynamic sliding of frictionally held bimaterial interfaces subjected to impact shear loading. *Proceedings of the Royal Society A: Mathematical, Physical and Engineering Sciences*, *462*(2074), 2997–3026. doi: 10.1098/rspa.2006.1703

Pinton, G., Dahl, J., & Trahey, G. (2005, June). Rapid Tracking of Small Displacements with Ultrasound. In *IEEE Ultrasonics Symposium, 2005.* (Vol. 4, pp. 2062–2065). IEEE. Retrieved from http://ieeexplore.ieee.org/document/1603285/ doi: 10.1109/ULTSYM.2005.1603285

Pujol, J. (2003, March). The Body Force Equivalent to an Earthquake: A Tutorial. *SRL*, *74*(2), 163–168. Retrieved from https://pubs.geoscienceworld.org/srl/article/74/4/440/142890 doi: 10.1785/gssrl.74.2.163

Reid, H. (1910). The California Earthquake of April 18, 1906, Report of the State Earthquake Investigation Commission, The Mechanism of the Earthquake. *Nature*, *2*(2128), 165–166. doi: 10.1038/084165a0

Rosakis, A. J., & Coker, D. (1999). Cracks Faster than the Shear Wave Speed. *Science*, *284*(May), 1337–1340.

Rubino, V., Lapusta, N., & Rosakis, A. J. (2022, June). Intermittent lab earthquakes in dynamically weakening fault gouge. *Nature*, 1–8. Retrieved 2022-06-07, from https://www.nature.com/articles/s41586-022-04749-3 doi: 10.1038/s41586-022-04749-3

Rubino, V., Rosakis, A. J., & Lapusta, N. (2020). Spatiotemporal Properties of Sub-Rayleigh and Supershear Ruptures Inferred From Full-Field Dynamic Imaging of Laboratory Experiments. *Journal of Geophysical Research: Solid Earth*, *125*(2), 1–25. doi: 10.1029/2019JB018922

Shlomai, H., & Fineberg, J. (2016). The structure of slip-pulses and supershear ruptures driving slip in bimaterial friction. *nature communications*, *7*, 1–7. Retrieved from http://dx.doi.org/10.1038/ncomms11787 doi: 10.1038/ncomms11787

Trottet, B., Simenhois, R., Bobillier, G., van Herwijnen, A., Jiang, C., & Gaume, J. (2022, January). *Transition from sub-Rayleigh anticrack to supershear crack propagation in snow avalanches.* Retrieved 2022-01-20, from https://www.researchsquare.com/article/rs-963978/v1 doi: 10.21203/rs.3.rs-963978/v1

Umlauft, J., Lindner, F., Roux, P., Mikesell, T. D., Haney, M. M., Korn, M., & Walter, F. T. (2021). Stick-Slip Tremor Beneath an Alpine Glacier. *Geophysical Research Letters*, *48*(2), e2020GL090528. Retrieved 2022-06-17, from https://onlinelibrary.wiley.com/doi/abs/10.1029/2020GL090528 doi: 10.1029/2020GL090528

van Otterloo, J., & Cruden, A. R. (2016, June). Rheology of pig skin gelatine: Defining the elastic domain and its thermal and mechanical properties for geological analogue experiment applications. *Tectonophysics*, *683*, 86–97. Retrieved 2021-12-29, from https://www.sciencedirect.com/science/article/pii/S0040195116302256 doi: 10/f82rbq

2 References from the supplementary material

References

Aki, K., & Richards, P. G. (2009). Quantitative seismology. In *Book* (Second ed., p. 700). University Science Books.

Andrews, D. J., & Ben-Zion, Y. (1997). Wrinkle-like slip pulse on a fault between different materials. *Journal of Geophysical Research: Solid Earth*, *102*(B1), 553–571. doi: 10.1029/96JB02856

Pinton, G., Dahl, J., & Trahey, G. (2005, June). Rapid Tracking of Small Displacements with Ultrasound. In *IEEE Ultrasonics Symposium, 2005.* (Vol. 4, pp. 2062–2065). IEEE. doi: 10.1109/ULTSYM.2005.1603285

Sandrin, L., Catheline, S., Tanter, M., Hennequin, X., & Fink, M. (1999, October). Time-Resolved Pulsed Elastography with Ultrafast Ultrasonic Imaging. *Ultrasonic Imaging*, *21*(4), 259–272. doi: 10.1177/016173469902100402

Supporting Information for ”Dynamic full-field imaging of rupture radiation: Material contrast governs source mechanism”

Aichele J.[1,2] *, Latour S.[3], Roux P. [2]and Catheline S.[1]

[1]Laboratory of Therapeutic Applications of Ultrasound, INSERM & University of Lyon, Lyon, France

[2]ISTerre, Univ. Grenoble Alpes, Univ. Savoie Mont Blanc, CNRS, IRD, Univ. Gustave Eiffel, Grenoble, France

[3]Institute of Astrophysics and Planetology, IRAP & University of Toulouse III, Toulouse, France

Contents of this file

Additional Supporting Information (Files uploaded separately)

---

*currently at Department of Earth Sciences, Institute of Geophysics, Swiss Federal Institute of Technology, Zürich, Switzerland

1. Wave propagation video of the strong interface experiment. Contains the whole two second long acquisition.

2. Wave propagation video of the weak interface experiment. Contains the whole two second long acquisition.

3. Caption for video S1

4. Captions for video S2

1. Introduction

Section 2 contains a detailed description of the experimental setup, experimental workflow and the imaging methodology used to acquire the data presented in the main article, supplemented by Table S1. A detailed description of the analytic simulations, including the governing Green's functions are given as well. The simulation source parameters are visualized by means of additional plots Figs. S10 to S14. Supporting data is given in Section 4 and the two supplementary videos. The two videos show the particle velocities acquired throughout the entire experiments, from which all figures showing experimental results in the main article are derived. All additional figures showing experimental results are also derived from these two datasets of the strong and weak bimaterial experiment.

2. Detailed Materials & Methods

2.1. Samples

We use homemade polyvinyl-alcohol (PVA) hydrogels. These gels are commonly used to mimic biological tissue. In comparison with gelatin and agar-gels they have the advantage of a much longer lifetime if stored in water. The production process consist of the following consecutive steps:

- Solution of PVA-powder in hot water under constant stirring.
- Addition of 0.1-0.5 % of graphite powder to introduce the scatterers that assure the ultrasonic speckle.
- Rapid cool-down in an ice-bath of the viscous solution until gelification sets in.
- Freezing at $-18\,°C$ until complete gelification is reached.
- Complete thawing of the gel.

The last two steps are repeated until the gel has the desired elasticity. It should be noted, that the homemade gels are not homogeneous. During the production of the large samples required for the setup, incomplete solution of the PVA-powder could not be avoided and the long time needed for complete solidification led to deposition of graphite and PVA-powder at the bottom of the gel.

2.2. Friction bench

The motor is a Kollmorgen® AKM™ stepper motor, depicted in Fig. S1. It is piloted through a LabVIEW (National Instruments, Austin, TX, USA) interface which ensures synchronization with the imaging device. The motor drives an endless screw, which in turn drives a glass plate through a wagon that is sliding on low-resistance bills on two rails. The motor controls the rotation rate of the screw and thus the driving speed of the wagon. The movement of the glass plate and the friction of the asperity lead to deformation of a hydrogel, which is hold in a fixed position on the friction bench.

2.3. Asperity

We focus on a spatially limited sand asperity that gives rise to granular friction. A small patch of fine to medium sand (<0.5 mm), is placed on the glass plate in the center of the hydrogel position. The sand is not completely dry, because PVA hydrogels loose water, especially under stress. This becomes evident in the cohesion of sand grains after the experiment.

2.4. Imaging device

The imaging probe is a 128-element L7-4 (Philips) ultrasound probe centered at 5 MHz. The probe is connected to a high-frame rate ultrasound scanner (Verasonics Vantage™) which works at up to 10 000 frames per second. The host computer ensures sequence programming as well as registration and treatment of the acquired data through a Matlab™ interface. Each ultrasound frame is obtained through emission of plane waves as in Sandrin, Catheline, Tanter, Hennequin, and Fink (1999) and beamforming of the backscattered signals.

2.5. Imaging method

In order to visualize the wave propagation, we apply phase-based motion estimation on subsequent beamformed ultrasound frames (Pinton et al., 2005). Similar to ultrasound Doppler techniques, the retrieved US phase difference gives the relative shear wave displacement in the micrometer range.

This phase shift or phase difference can be expressed through the Fourier shift theorem. The theorem states, that a signal $x(t)$ delayed by dt has a Fourier transform that equals the Fourier transform of $x(t)$ multiplied by $e^{-j\omega dt}$. Hence, $x(t-dt) \leftrightarrow e^{-j\omega dt}\hat{x}(\omega)$.

Because for beamformed ultrasound reflection images (IQ), only displacements in direction of the plane ultrasound wave can be recorded, the translation of the ultrasound reflection images is one-dimensional. The spatial coordinates along the axis of ultrasound propagation (z) are inferred from the ultrasonic travel-time and the central frequency of the probe. With a time difference dt of snapshots t_1 and t_2 and US travel-time τ ($z \rightarrow \tau$) the theorem reads:

$$IQ(x,\tau,t_2) = IQ(x,\tau - d\tau, t_1) \tag{1}$$

$$\hat{IQ}_2(\xi,\omega,t_2) = e^{-j2\pi(\omega d\tau)}\hat{IQ}(\xi,\omega,t_1) \tag{2}$$

The phase shift $e^{-j2\pi(\xi d\tau)}$ is calculated by using the normalized cross power spectrum, which is retrieved through multiplication with the complex conjugate in the Fourier domain.

$$e^{-j2\pi(\omega d\tau)} = \frac{\hat{IQ}(\xi,\omega,t_1)\hat{IQ}^*(\xi,\omega,t_2)}{\left|\hat{IQ}(\xi,\omega,t_1)\hat{IQ}(\xi,\omega,t_2)\right|} \tag{3}$$

The argument of equation 3 gives thus the relative displacement between two images in radians and the particle velocity reads:

$$v_p(x,\tau) = \frac{c_0}{(4\pi f_c)}\arg(e^{-j2\pi(\omega d\tau)}) \tag{4}$$

- with τ being related to the spatial coordinate z by $\lambda = \frac{c_0}{f_c}$ and z being resolved by the imaging system at four points per US wavelength.

- with c_0 being the speed of ultrasound, approximately $1480\,\mathrm{m\,s^{-1}}$ (speed of sound in water) in soft matter, and f_c being the central frequency of the probe.

In the IQ domain, the correlation is thus a simple point by point multiplication in the frequency domain and time-consuming windowing is not required. Due to the very high resolution of the probing ultrasound waves of 3×10^{-5} m and the high frame rate, the retrieved particle velocity can be locally integrated over time to get the total displacement along the ultrasound propagation direction. Furthermore, taking the spatial gradient of the accumulated displacement allows for estimation of one component of the strain tensor. Likewise, time differentiation leads to particle acceleration which is advantageous when continuous deformation masks simultaneous wave propagation.

2.6. Unidirectional shear force

The particle displacement in the direction i inside a homogeneous body due to a unidirectional shear force in the direction j is given by the convolution of the source time function $X_0(t)$ with the medium's Green's function G_{ij}:

$$
\begin{aligned}
u_i(\vec{x},t) &= X_0 * G_{ij} \\
&= \frac{1}{4\pi\rho}(3\gamma_i\gamma_j - \delta_{ij})\frac{1}{r^3}\int_{\frac{r}{a}}^{\frac{r}{b}} \tau X_0(t-\tau)d\tau \\
&+ \frac{1}{4\pi\rho\alpha^2}\gamma_i\gamma_j\frac{1}{r}X_0(t-\frac{r}{\alpha}) \\
&- \frac{1}{4\pi\rho}\beta^2(\gamma_i\gamma_j - \delta_{ij})\frac{1}{r}X_0(t-\frac{r}{\beta}),
\end{aligned}
\tag{5}
$$

where r is the distance from the source to the receiver, ρ is density, α and β are the compression and shear wave speeds, τ is the source time and δ_{ij} is the kronecker symbol. γ_i is defined as $\gamma_i = \frac{x_i}{r}$. A thorough derivation is given in Chapter 3 and 4 of Aki and Richards (2009).

2.7. Double-couple point source

The displacement field induced by a shear dislocation can be described as a convolution of the seismic moment tensor with the Green's function. Using summation convention, the n-th displacement component is expressed as $u_n = M_{pq} * G_{np,q}$, with $M_0(t) = \mu\bar{u}(t)A$, where $\bar{u}$ is the averaged displacement discontinuity from the shear displacement, A is fault area and μ is shear modulus. The time dependant point force function $X_0(t)$ for the unidirectional shear force has thus its equivalent for the DC in the material and slip area dependant displacement function $M_0(t)$. In polar coordinates with the DC location as origin, and vector form, the displacement due to a double-couple source reads:

$$\begin{aligned} u(\vec{x},t) = {} & \frac{1}{4\pi\rho}\vec{A}^N \frac{1}{r^4}\int_{\frac{r}{a}}^{\frac{r}{b}} \tau M_0(t-\tau)d\tau \\ & + \frac{1}{4\pi\rho\alpha^2}\vec{A}^{IP}\frac{1}{r^2}M_0(t-\frac{r}{\alpha}) + \frac{1}{4\pi\rho\beta^2}\vec{A}^{IS}\frac{1}{r^2}M_0(t-\frac{r}{\beta}) \\ & + \frac{1}{4\pi\rho\alpha^3}\vec{A}^{FP}\frac{1}{r}\dot{M}_0(t-\frac{r}{\alpha}) + \frac{1}{4\pi\rho\beta^3}\vec{A}^{FS}\frac{1}{r}\dot{M}_0(t-\frac{r}{\beta}), \end{aligned} \tag{6}$$

94 where the notation is equivalent to Eq. (5). The radiation patterns of the near field and the

95 far and intermediate compression (P) and shear (S) field terms are described by:

$$\begin{aligned} \vec{A^N} &= 9\sin 2\theta\cos\phi\vec{\hat{r}} - 6(\cos 2\theta\cos\phi\vec{\hat{\theta}} - \cos\theta\sin\phi\vec{\hat{\phi}}) \\ \vec{A^{IP}} &= 4\sin 2\theta\cos\phi\vec{\hat{r}} - 2(\cos 2\theta\cos\phi\vec{\hat{\theta}} - \cos\theta\sin\phi\vec{\hat{\phi}}) \\ \vec{A^{IS}} &= -3\sin 2\theta\cos\phi\vec{\hat{r}} - 3(\cos 2\theta\cos\phi\vec{\hat{\theta}} - \cos\theta\sin\phi\vec{\hat{\phi}}) \\ \vec{A^{FP}} &= \sin 2\theta\cos\phi\vec{\hat{r}} \\ \vec{A^{FS}} &= \cos 2\theta\cos\phi\vec{\hat{\theta}} - \cos\theta\sin\phi\vec{\hat{\phi}}, \end{aligned}$$

96 where ϕ, θ and r are the spherical coordinates, with ϕ being the angle to the direction of the

97 DC and θ being the angle to the orthogonal of the DC direction.

2.8. Kinematic simulations

The propagating ruptures are modeled by superposing unidrectional shear point forces or double-couple point forces in space and time. The same source function $X_0(t)$ or $M_0(t)$ is therefore shifted in x-direction and time according to the rupture speed profile. Along the prescribed rupture surface, each grid point, which is spaced at 0.3 mm acts thus as a point source, emitting at different times. We assume an axisymmetric setup and homogeneous medium and extract the wavefield in a $x - z$ plane for the simulation. As a consequence, the physical rupture surface of the experiment is reduced to a rupture line in the simulation. The only processing undertaken for visualization of the simulations is a median filter which was applied to the simulations in space in order to visually highlight the coherent wavefronts. This is due to the fact that the simulations were undertaken with an equivalent resolution in x and z while the experiment was acquired at a higher spatial resolution in z. Point source functions for the kinematic simulations and rupture speed profile resulting from the superposition of these point sources in time and space can be found in Figs. S10 to S14. The actual wavefield is retrieved by convolving the derivative with the Green's function and integrating the resulting wavefield to avoid non-smooth or long source functions in the computation. Note that the simulations are qualitative and the source amplitudes are normalized.

2.9. Wave and rupture speed measurements

Examples of the manual time of flight measurements from the strong bimaterial interface experiment are given in Figs. S15 and S16. The given uncertainty stems from the time resolution of the data acquisition. An example of the speed estimation from the supershear front, as described in the main article, is shown in Fig. S17.

3. Supplementary table

Table S1. Experimental parameters for the experiments presented in Fig. 2-5 (main article).

Experiment Ref.	**Gel** Nr.	**PRF** $[\frac{frame}{s}]$	**Drive speed** $[\frac{mm}{s}]$	**Normal load** $[kg]$	**Duration** [s]
Fig. 2-3	Gel 1	3000	1	≈ 4.0	2
Fig. 4-5	Gel 1+2	3000	2	≈ 2.5	3

4. Supplementary figures

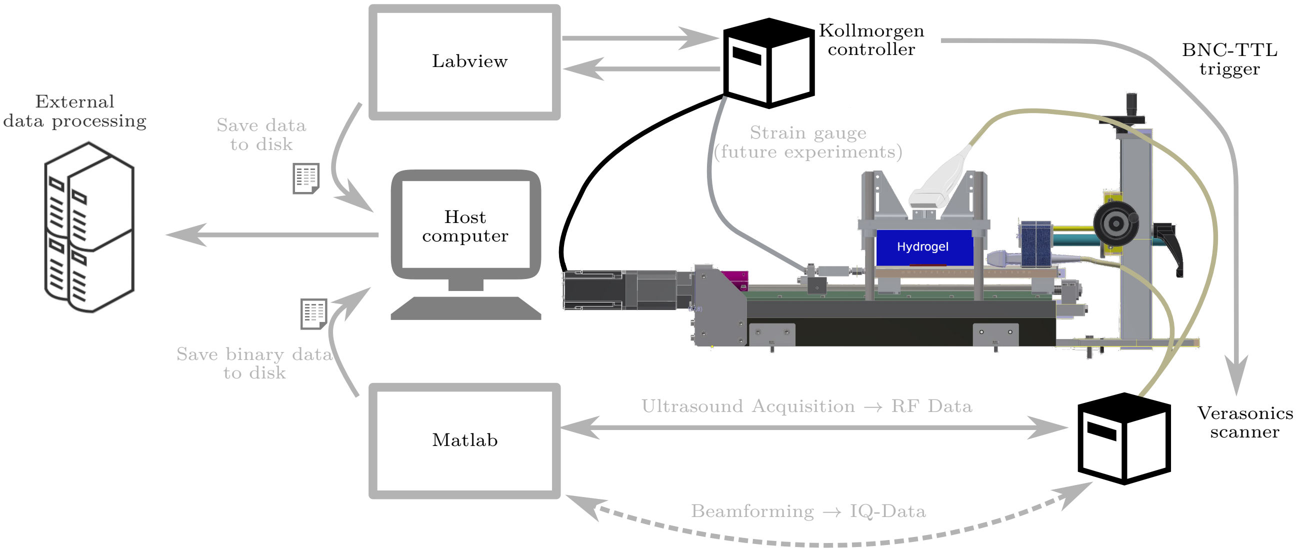

Figure S1. Experimental workflow: Raw-data acquisition, beamforming and post-processing are separate processes. This permits rapid succession of experiments. The length of the experiment is hereby only limited by the frame size of the raw data and the available memory of the host computer. Labview pilots the motor and triggers the ultrafast scanner via a BNC-TTL trigger. Center sketch: Friction bench. From left to right: A stepper motor drives an endless screw which displaces the wagon with the glass plate. A hydrogel is posed on the glass plate with a frictional layer of sand in between. Normal load is applied on top via weights. The gel is blocked in the direction of movement of the plate and a small part at the bottom is left free to deform. An ultrasound imaging probe is placed on the side or top of the gel with a layer of echography gel in-between to ensure coupling and omit stress induced by the probe. In this paper only the vertical probe position is investigated.

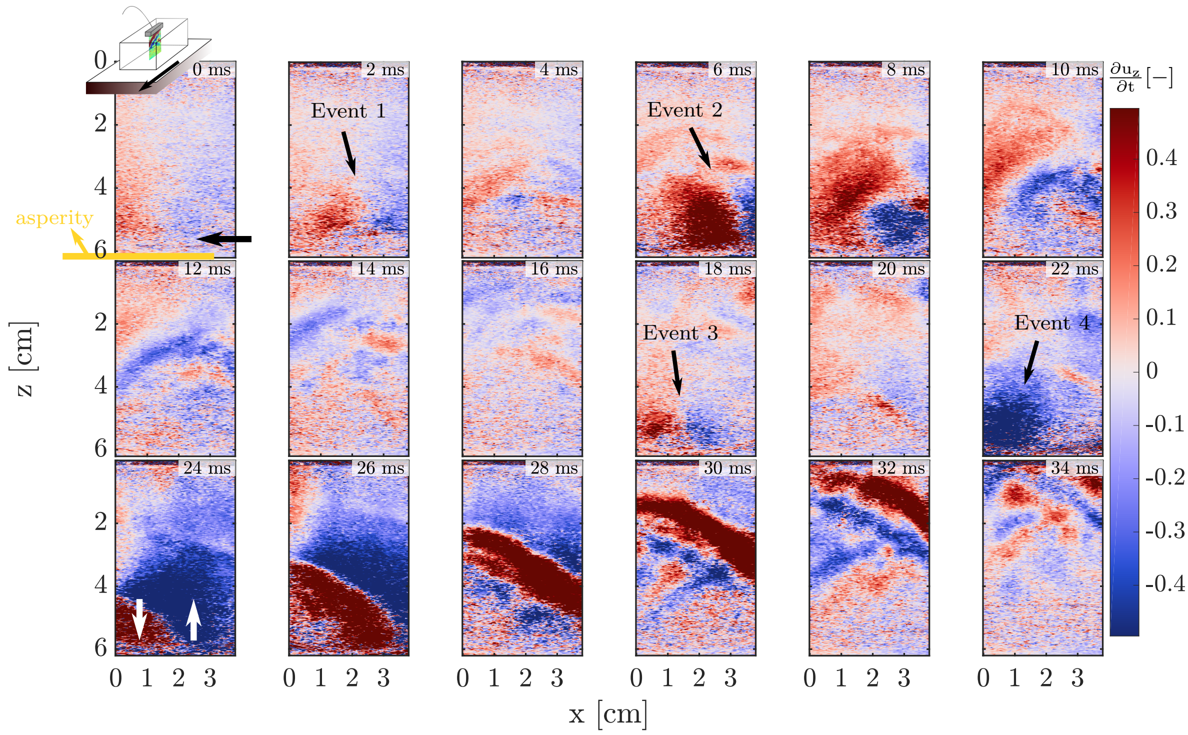

Figure S2. Particle velocity snapshots of a 34 ms long extract of the glass-hydrogel experiment (strong bi-material contrast). The direction of the plate movement is indicated by a black arrow in the first snapshot. The schematic experimental setup with the probe position is indicated by the inset in the same snapshot. Note that blue color denotes upwards polarization of the z-component of the particle velocity and red denotes downwards polarization of the z-component of the particle velocity. Event 3 corresponds to the localized event of figure Fig. 2 (main article) and event 4 to the rupture propagation across the whole asperity of Fig. 3 (main article)

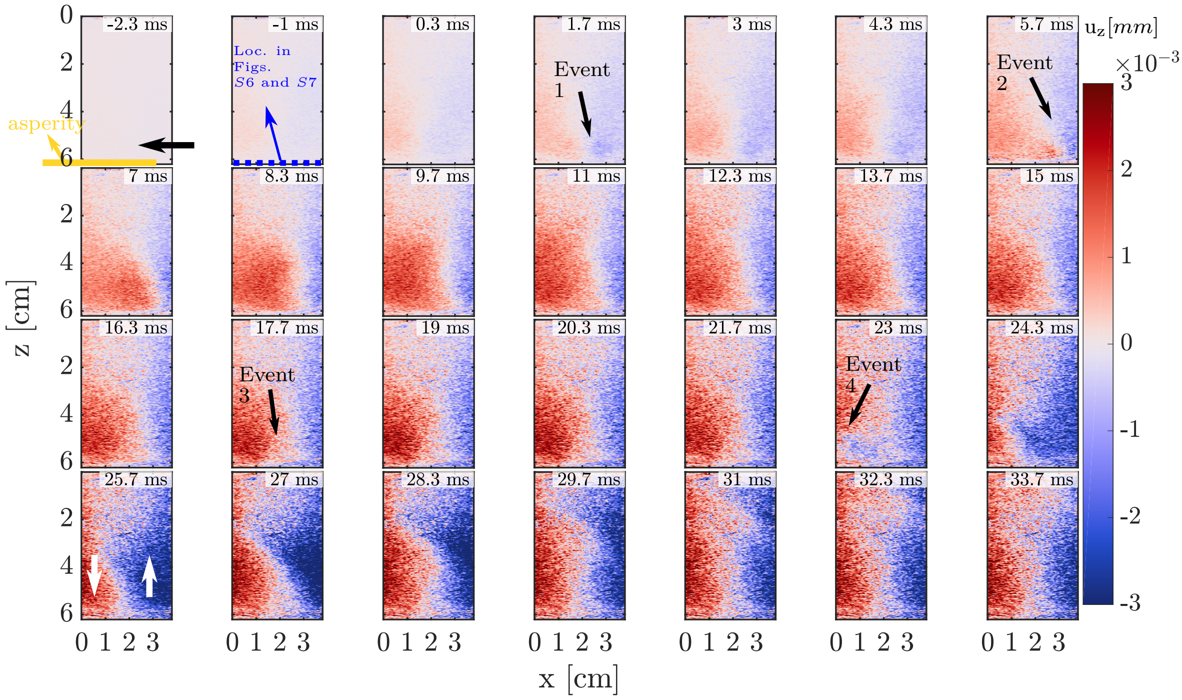

Figure S3. The cumulative displacement of the rupture cycle of Fig. S2 relative to −2.3 ms. The blue points in snapshot 2 indicate the approximate locations of the 1D displacement curves in Figs. S6 and S7. The three precursory events (1, 2 and 3) nucleate at the point of stress concentration, where the fault normal displacement changes sign. The supershear rupture however nucleates outside the imaging region and possibly not at a visible point of stress concentration. Note how the displacement field from 23 ms resembles a propagating slip pulse as computed by Andrews and Ben-Zion (1997).

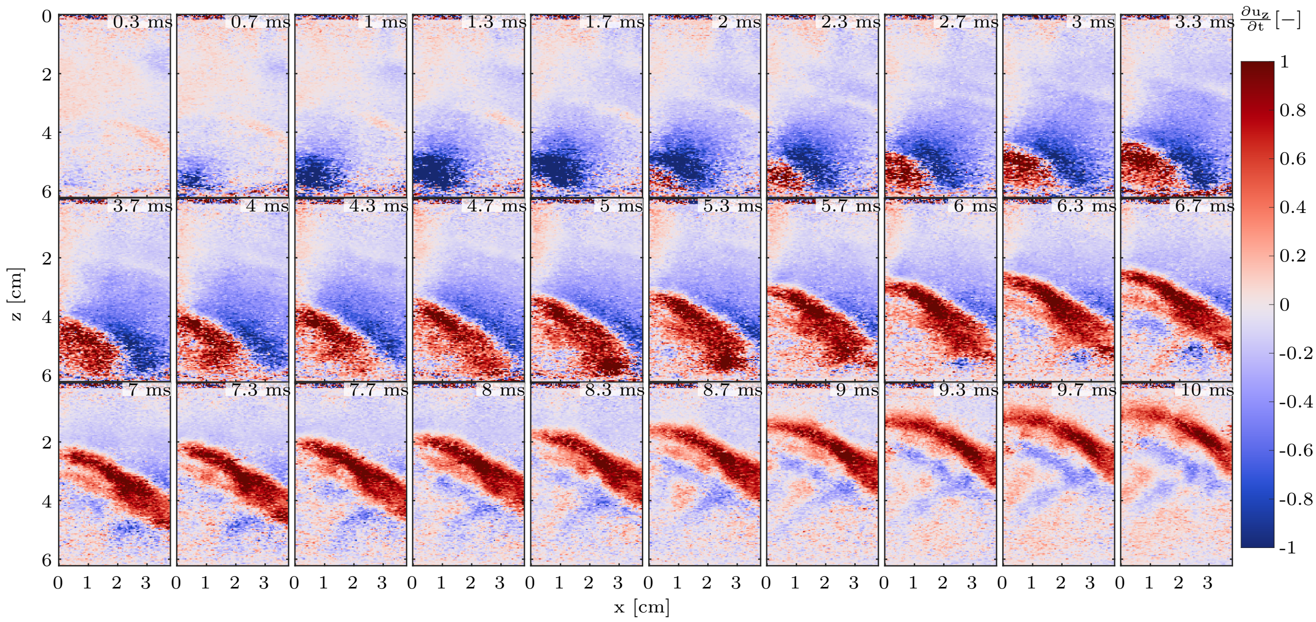

Figure S4. High temporal resolution particle velocity snapshots of the event in Fig. 3 (a) (main article). In contrast to Fig. 3 (a) (main article), the displayed snapshots are shown at the experimentally acquired temporal resolution.

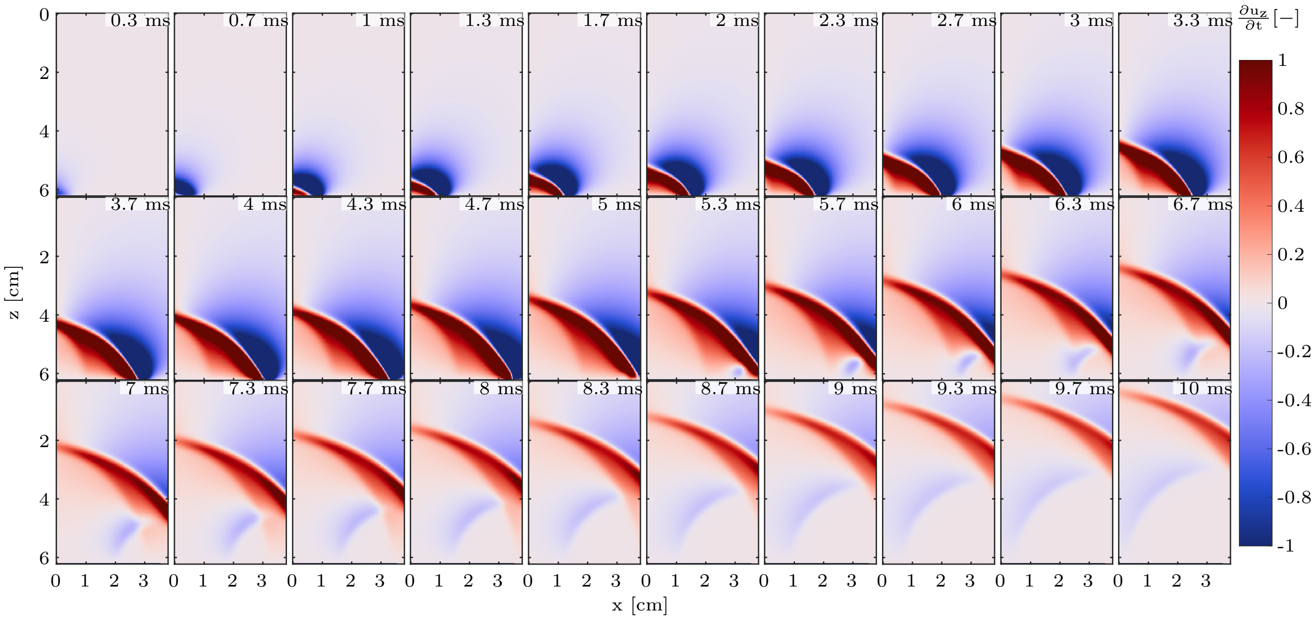

Figure S5. High temporal resolution particle velocity snapshots of the simulation in Fig. 3 (b) (main article). In contrast to Fig. 3 (a) and (b) (main article), the displayed snapshots are shown at the experimentally acquired temporal resolution.

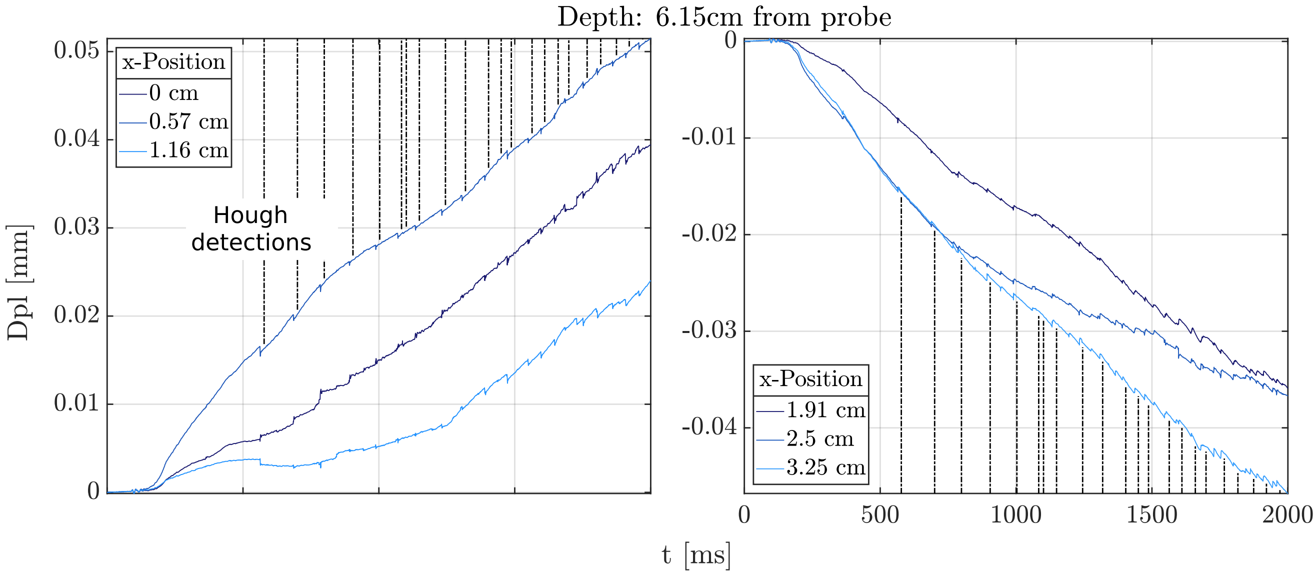

Figure S6. Displacement curves of the entire experimental time during the glass-hydrogel experiments for selected points on the rupture surface. Positive is downwards displacement, away from the probe as in Fig. S3. The overall trend is continuous deformation of the gel. The black dashed lines indicate successful supershear front detections by image segmentation and the Hough transform. Each sawtooth in the displacement curves thus represents a rupture as the one zoomed in on Fig. S7.

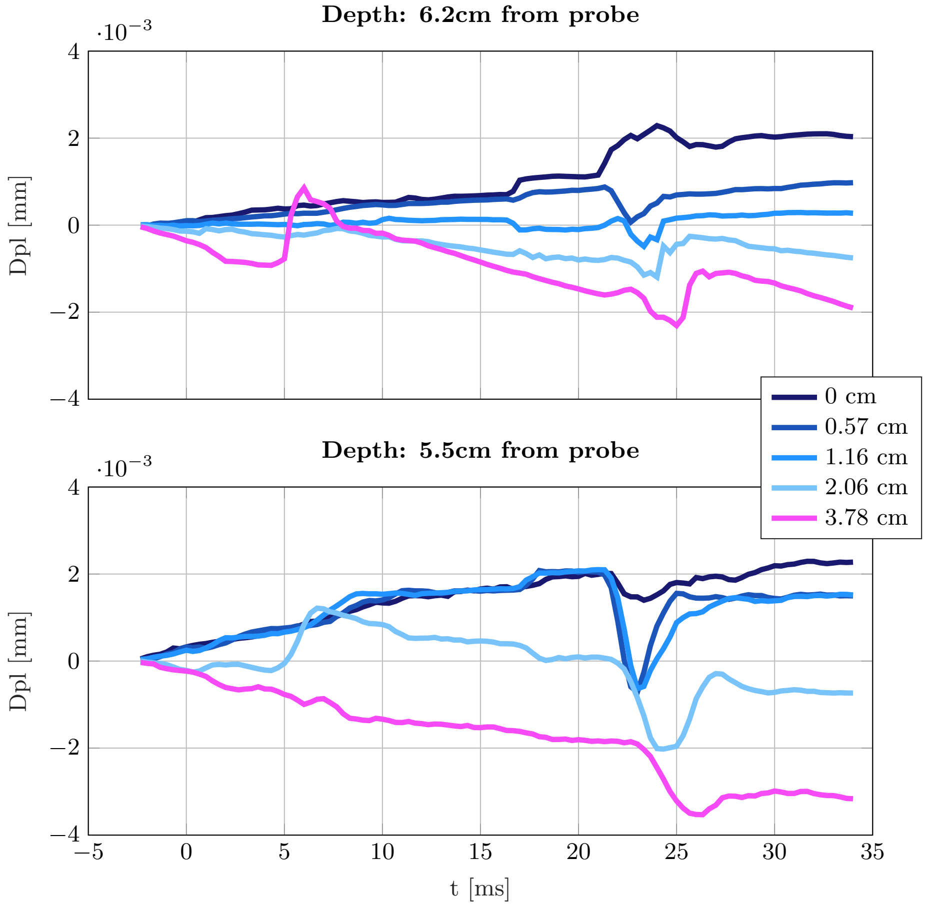

Figure S7. Cumulative z-displacement, calculated as the cumulative sum of the z-component of the measured particle velocity. All curves are taken at a specified x-location and plotted against time. Displacement against time for several points along x on the rupture surface. The points are as close as possible to the fault, possibly partly inside the granular material. Positive is downwards displacement, away from the probe as in Fig. S3. The cycle from Fig. S3 is shown. In the displacement, the time-space evolution of the slip, whose dynamics are shown in Fig. S4, becomes evident. Note the event at x=2.06 cm x=3.78 cm and 6 ms. It represents Event 2 of Figs. S2 and S3.

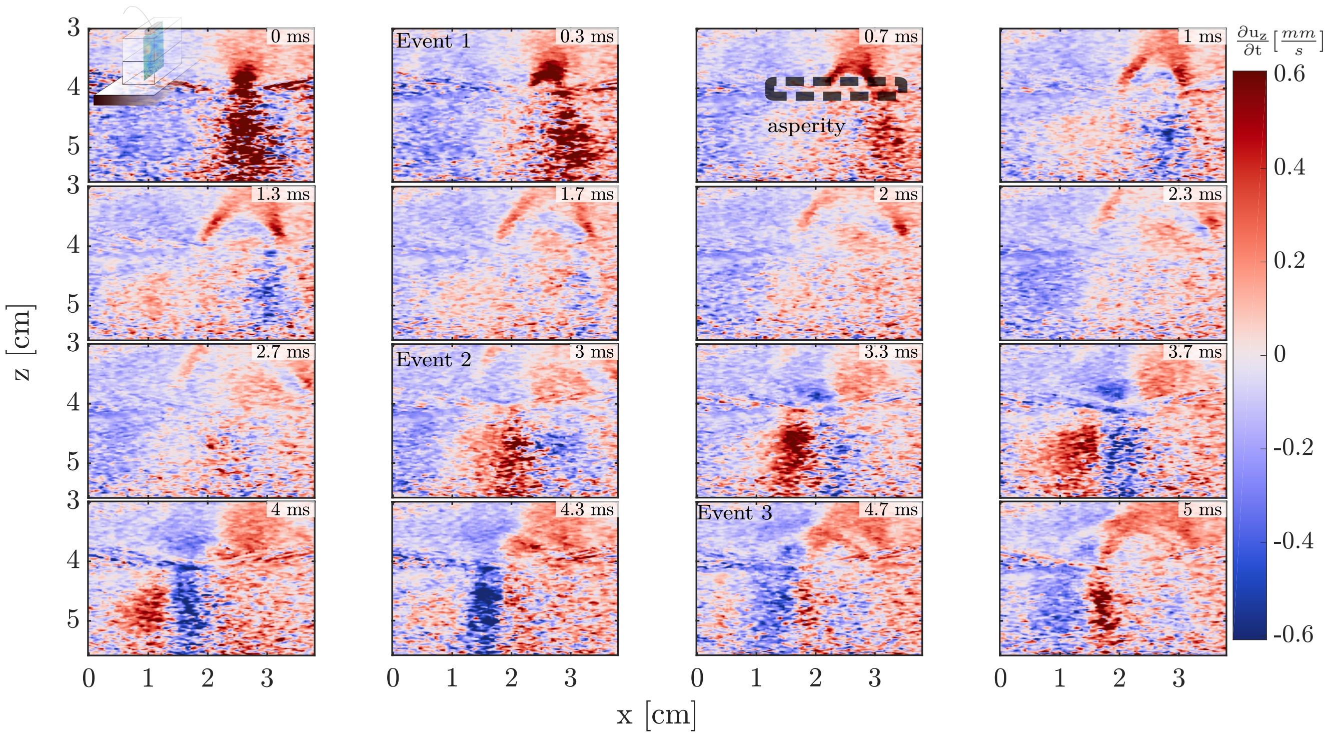

Figure S8. Particle velocity snapshots during an extract of the gel-gel rupture experiment (weak material contrast). Event 1 corresponds to the rupture propagation that is studied in Fig. 5 (main article) and event 2 to the localized event of figure Fig. 4 (main article).

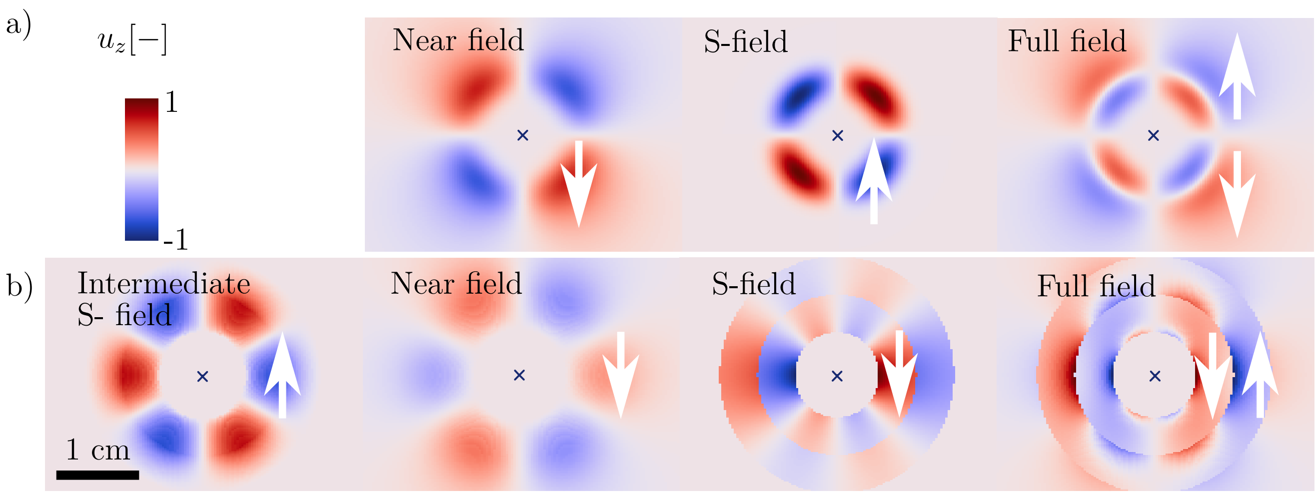

Figure S9. Radiation patterns for the $z-$component of the Green's functions for a right-pointing unidirectional shear force and a right-pointing double-couple. a) Displacement field of a point source resulting from the convolution of a Gaussian force in time with the Green's function of a unidirectional shear force (Eq. (5)). b) Particle velocity field of a point source resulting from the convolution of a ramp displacement in time with the Green's function of a double couple of forces (Eq. (6)).

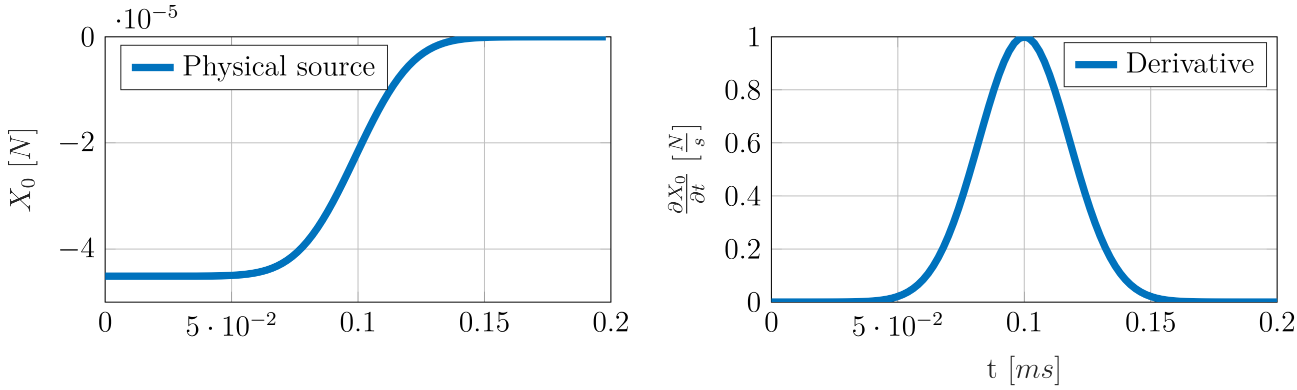

Figure S10. Source function for Fig. 2 (b) (main article).

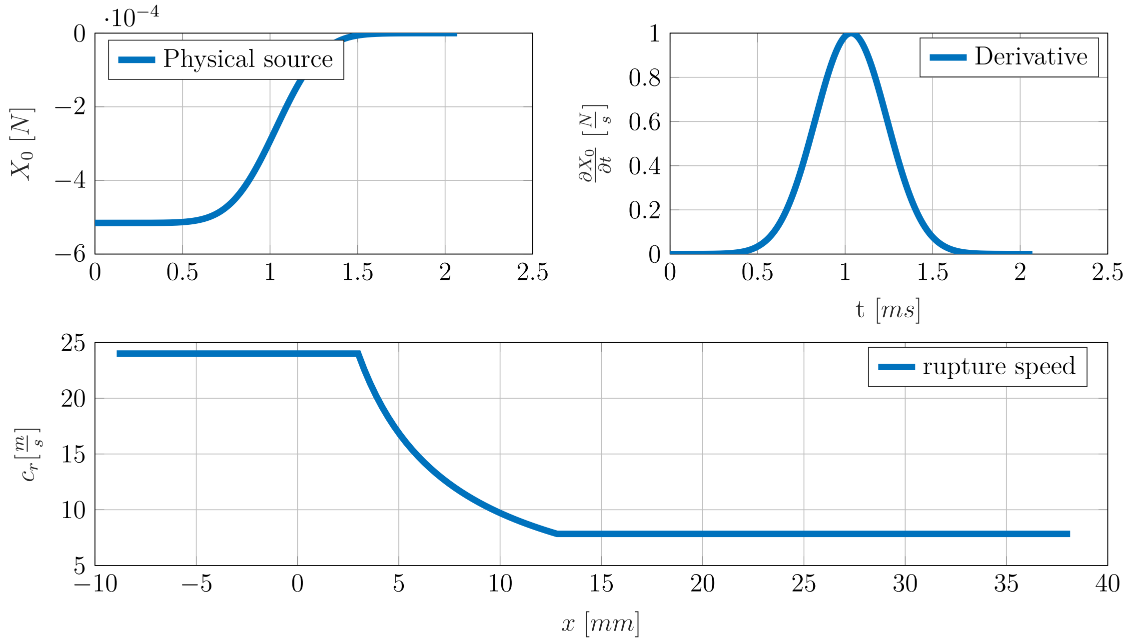

Figure S11. Top: Source function for Fig. 3 (b) (main article) and Fig. S5 (left) and its derivative (right). Bottom: Rupture speed profile in space. The rupture starts before the x-extension of the imaging plane.

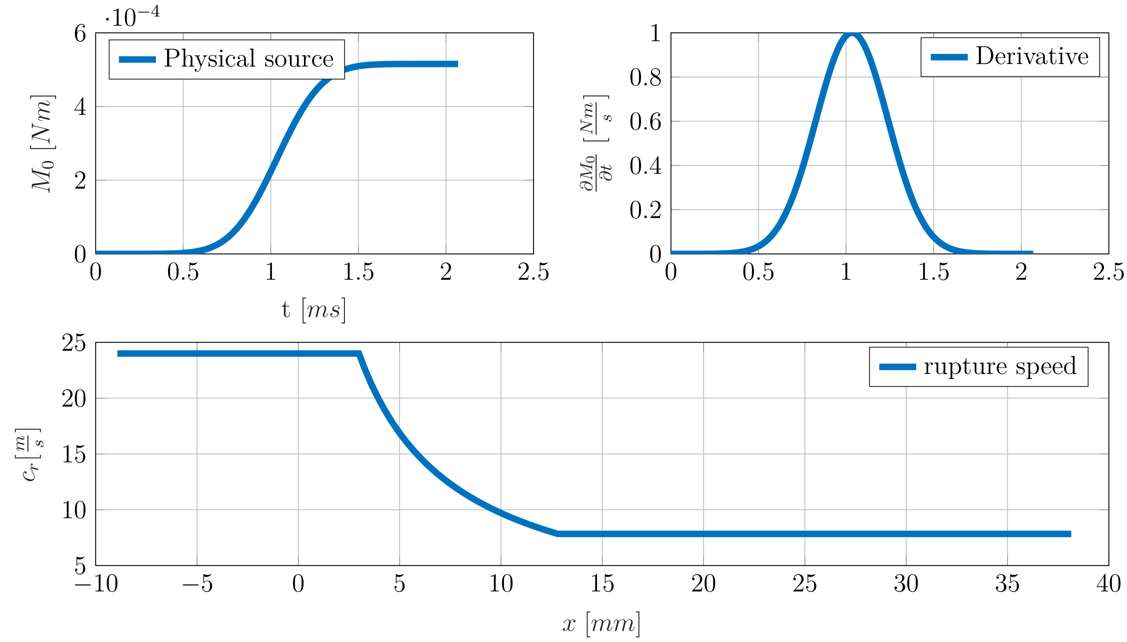

Figure S12. Source function for Fig. 3 (c) (main article) (left) and its derivative (right). Bottom: Rupture speed profile in space. The rupture starts before the x-extension of the imaging plane.

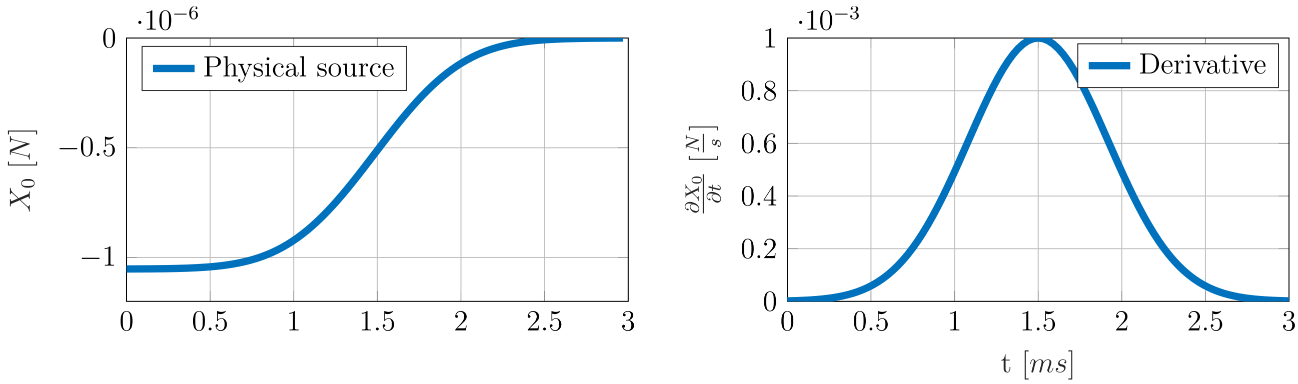

Figure S13. Source function for Fig. 4 (b) (main article).

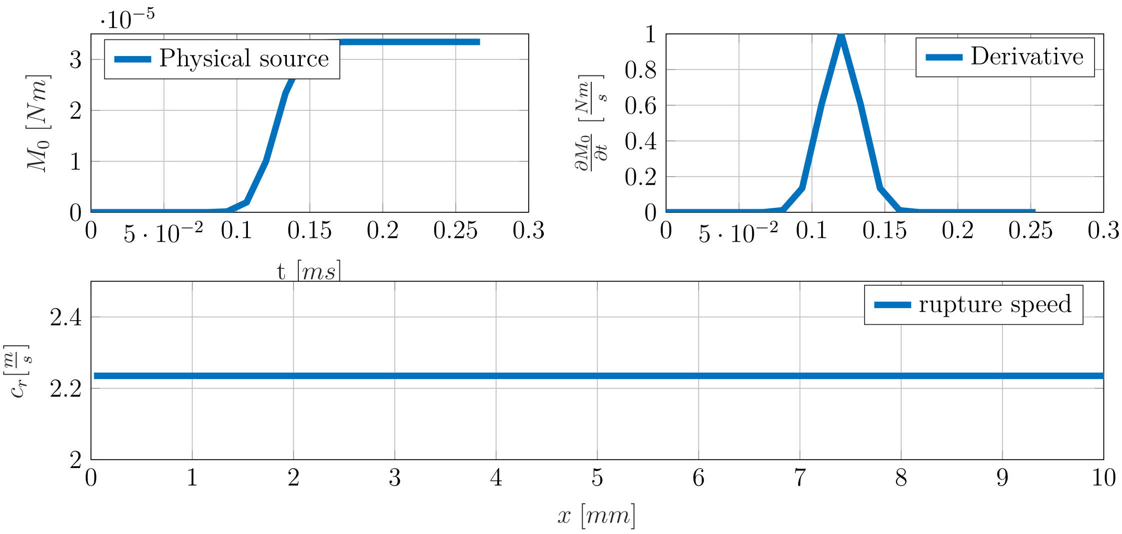

Figure S14. Source function for Fig. 5 (b) and (e)-(f) (main article).

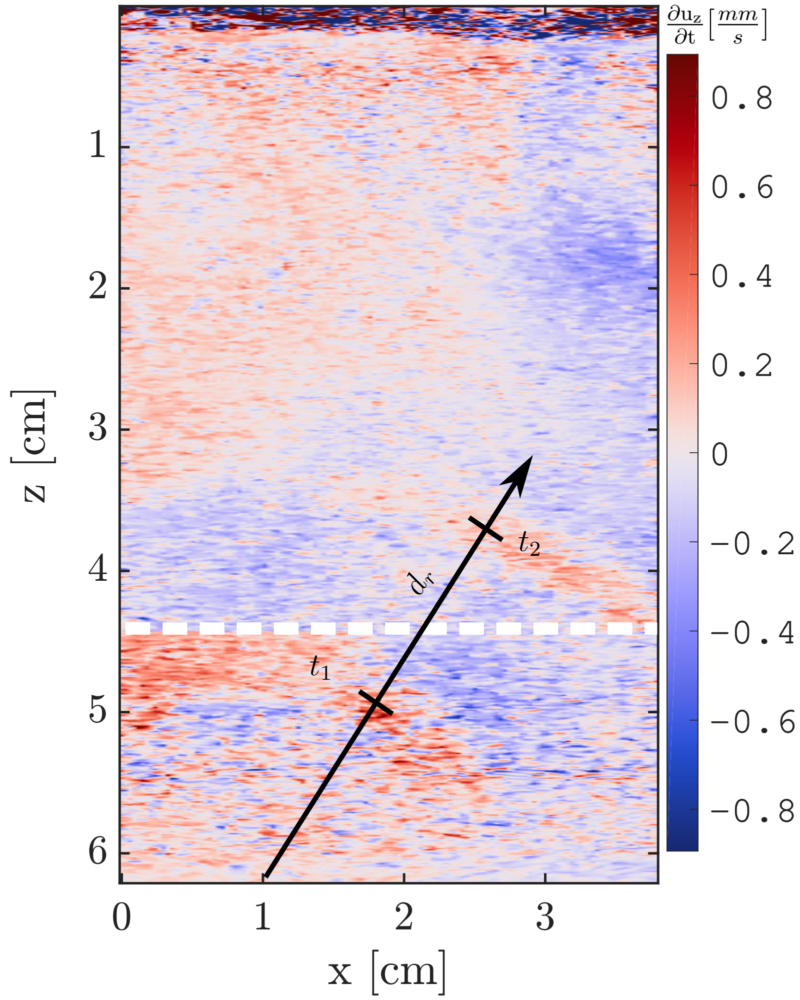

Figure S15. Shear wave time of flight on a composite image of two snapshots. The part below the white line shows a snapshot at t_1 and the upper part shows a snapshot at t_2. The shear wave speed is calculated from $v_s = \frac{dr}{t_2 - t_1}$ as $6.9 \pm 1\,\mathrm{m\,s^{-1}}$.

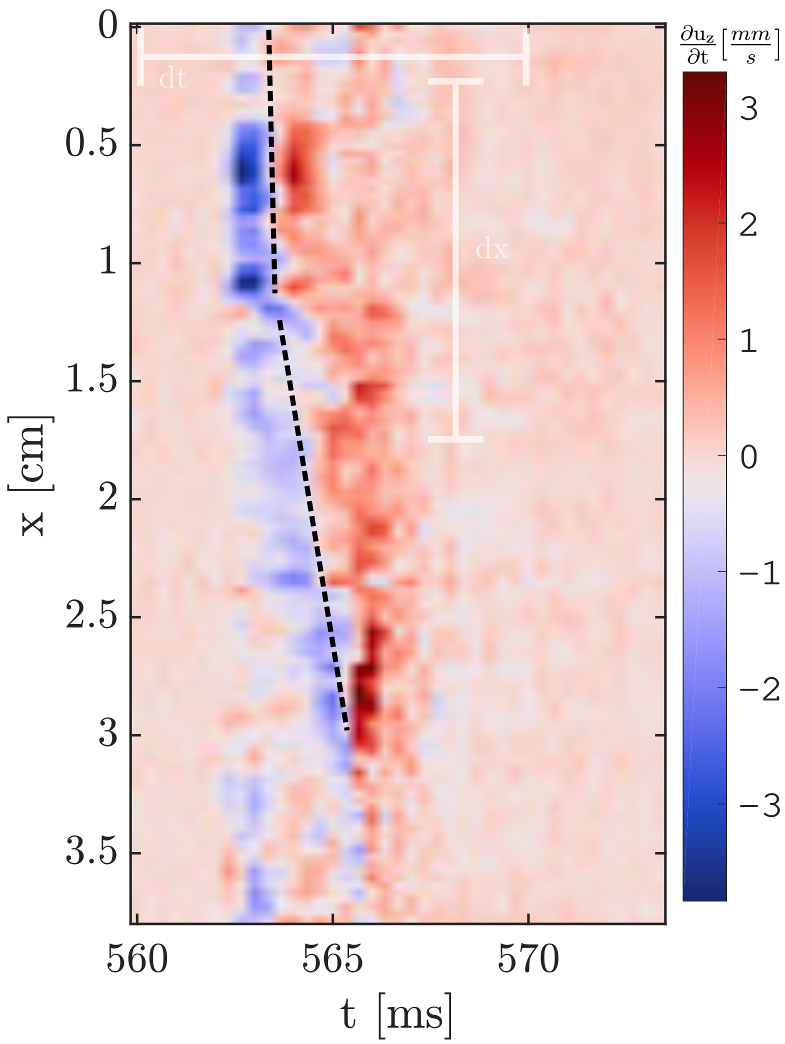

Figure S16. Example of the time of flight measurement of the rupture speed. The speed along the profile is not constant and the estimation by eye can only be tentative. The rupture speed equivalent to the black line on the indicated segment between 1.3 cm and 3 cm is calculated from: $v_r = \frac{dx}{t_2 - t_1}$, as $10.6 \pm 1\,\mathrm{m\,s^{-1}}$.

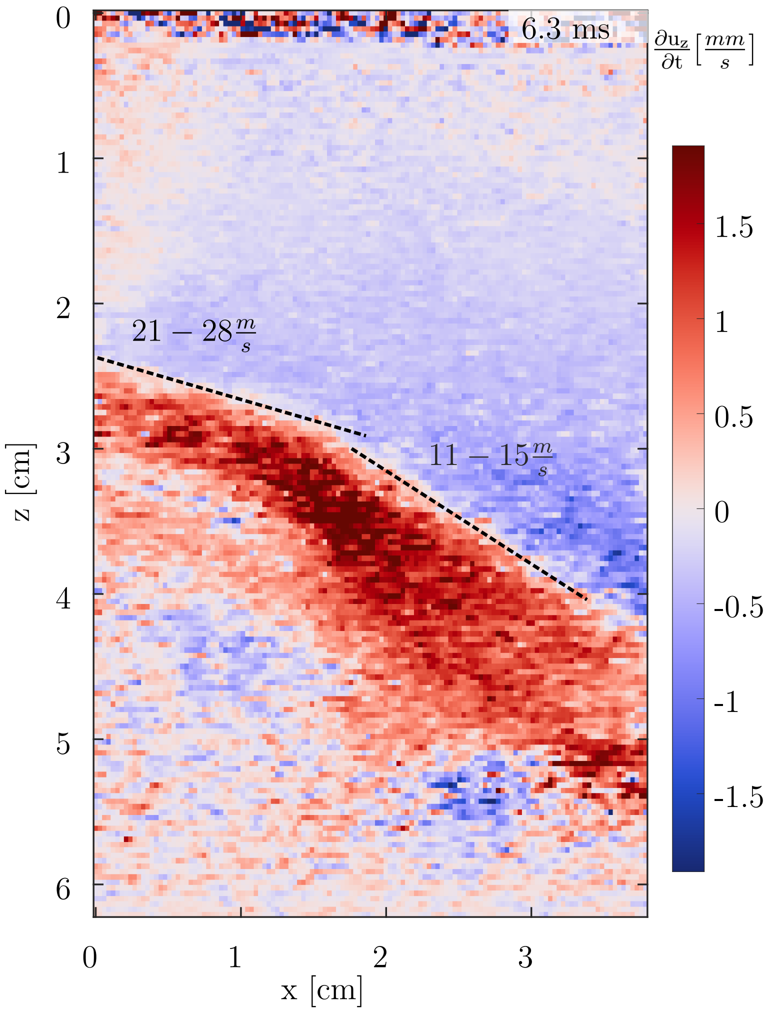

Figure S17. Example of the supershear front. Two slopes can clearly be identified, indicating a decelerating rupture. The rupture speed is calculated from the shear wave speed c_s and the angle to the horizontal β: $v_r = \frac{c_s}{sin(\beta)}$. The rupture speed corresponding to each segment of the supershear fron is indicated.

5. Additional Supporting Information Captions (Files uploaded separately)

5.1. Caption for video S1

Wave propagation video of the particle velocities of the entire strong bi-material experiment. Blue color is upwards pointing and red color is downwards pointing particle velocity. The imaging plane is $x - z$ as described in the main article. Note how the main ruptures resemble each other indicating a stick-slip behaviour. The video extract corresponding to Figs. 2-3 of the main article can be found from 770 - 800 ms.

5.2. Caption for video S2

Wave propagation video of the particle velocities of the entire weak bimaterial experiment. Blue color is upwards pointing and red color is downwards pointing particle velocity. The imaging plane is $x - z$ as described in the main article. Here, both halfspace are imaged, albeit imaging quality is superior above the interface. The video extract corresponding to Figs. 4-5 of the main article starts at approximately 2396 ms.

6. References

References

Aki, K., & Richards, P. G. (2009). Quantitative seismology. In *Book* (Second ed., p. 700). University Science Books.

Andrews, D. J., & Ben-Zion, Y. (1997). Wrinkle-like slip pulse on a fault between different materials. *Journal of Geophysical Research: Solid Earth*, *102*(B1), 553–571. doi: 10.1029/96JB02856

Pinton, G., Dahl, J., & Trahey, G. (2005, June). Rapid Tracking of Small Displacements with Ultrasound. In *IEEE Ultrasonics Symposium, 2005.* (Vol. 4, pp. 2062–2065). IEEE. doi: 10.1109/ULTSYM.2005.1603285

Sandrin, L., Catheline, S., Tanter, M., Hennequin, X., & Fink, M. (1999, October). Time-Resolved Pulsed Elastography with Ultrafast Ultrasonic Imaging. *Ultrasonic Imaging*, *21*(4), 259–272. doi: 10.1177/016173469902100402